

ALIGNMENT OF LIGHT AND MASS IN LENSING GALAXIES

Claudio Bruderer

Abstract

Understanding the structure and properties of galaxies today is essential to understand how galaxies formed. This poses a larger problem to us than one might imagine. Especially constraining the dark matter distribution in galaxy halos is not trivial. There are only a few methods to directly estimate this distribution. One of them is strong gravitational lensing, an effect caused by all of mass. This phenomenon allows constraining the gravitational potential of lens galaxies and thus the mass distribution. With knowledge of the light distribution it is possible to disentangle the dark matter and baryonic mass components and study their properties. We use the newly-developped nonparametric framework *GLASS* to model the mass distribution of a total of 15 strong gravitational lensing galaxies, most of which are early-type galaxies, for which we have information on the baryonic mass distribution. We are thus able to separate the mass components. By using a simple shape measure, namely the inverse of the moment of inertia tensor, we can analyze the shapes of the distributions. Analyzing the alignments between the semi-major axes of the distributions, we find that there can be significant misalignments and also cases of alignment between the semi-minor and semi-major axes. Mass thus need not follow light. Furthermore, the ellipticities of the dark matter distributions are always smaller than the baryonic mass distributions. Dark matter halos tend to be more spherical than the light distribution of the galaxy. We also consider the environment of the lenses. We find that lenses in denser environments tend to be more misaligned with either the semi-major or semi-minor axis. Additionally, the semi-major axis of lenses lying in groups or clusters of the dark matter halo might be oriented in direction of the centroid.

Contents

1	Introduction	2
2	Data	3
3	Method	6
3.1	GLASS	6
3.2	Priors and assumptions	6
3.3	Shape measure	8
4	Results	9
4.1	Lens Reconstruction	9
4.2	Misalignments between stellar and dark matter distributions	10
4.3	Ellipticities of stellar and dark matter distributions	10
4.4	Misalignments between the dark matter distributions and environment	10
5	Conclusion	11
REFERENCES		11
A	Reconstructed Lenses	13

1 Introduction

Gravitational lensing is one of the few phenomena that allow probing the matter distribution directly. It makes no distinction between baryonic and dark matter, both components act on light rays in the same way. Gravitational lensing is therefore somewhat special as it allows to 'see' dark matter, if we are able to separate the two components. Therefore studying these effects allows us to probe dark matter and its properties. We are typically interested in measuring its distribution, how it clusters, its connection to structure formation, and of course its nature. With strong gravitational lensing galaxies we are effectively probing the matter distribution on relatively small scales. Thus, much insight could be gained in how galaxies form and how they are structured.

The main challenges are however estimating first, the baryonic mass distribution, such that the two components can be disentangled, and second, modelling the lens, i.e. the mass distribution. We do not elaborate the first problem (see e.g. Leier (2011)) further but skip right ahead to the second problem. There are in general two classes of methods to reconstruct gravitational lenses, parametric and nonparametric methods. A comparison of these two classes of methods can be found in Coe et al. (2008). Parametric methods assume a distribution, which depends only on few parameters, such that a best-fitting model can be found. Nonparametric (or free-form) methods chose a specific base set. Due to the fact that there is no *a priori* reason to prefer certain mass models over others, given that they all satisfy certain prior conditions and reproduce the same gravitational lensing effects, there is no best-fitting model. It is therefore important to explore many models and look at the properties of all the models in the ensemble. We typically need to sample high-dimensional parameter spaces, which describe all allowed models, in a uniform and uncorrelated way to generate a representative sample. This is a computational challenge and certainly not trivial (Coles, 2008; Lubini & Coles, 2012). Parametric methods are usually computationally cheaper, but as the distributions are assumed beforehand, they might bias the result too much.

With these tools, we can start answering the question whether mass follows light. It is a well-known fact that for observations to match e.g. rotation curves and simulations, the radial density profiles of baryonic mass and dark matter differ. As we know that galaxies can be quite triaxial, the next question to ask is whether dark matter and baryonic matter need to be aligned and have similar ellipticities. If this is not the case, then this needs to be explained by mechanism and effects (e.g. environment of the lenses) that produce and sustain these different properties. It is furthermore unclear whether modified gravity theories introduced to explain the 'missing matter' could explain misalignments between mass and light.

There were already attempts to analyze the alignment of light and mass. Keeton et al. (1997) started looking at misalignments quite early on. They use Singular Isothermal Spheres (SIS) with an external shear term and Singular Isothermal Ellipsoids (SIE) (e.g. Kormann et al. (1994)) without external shear to model the mass distribution. Applying this to a sample of 17 lenses, they find a strong correlation between light and dark matter distributions, while there is only a small scatter of less than 10° , if there is no strong external perturbation. They find however no correlation between the axis ratios of the distributions.

Later on, Koopmans et al. (2006) and Gavazzi et al. (2012) analyzing lens samples of similar sizes and Treu et al. (2009) analyzing a lens sample containing even 70 galaxies also looked for misalignments. They all use SIEs to model the mass distributions. Only Gavazzi et al. (2012) however include an external shear contribution in case more information is available. They neglect the external shear although Keeton et al. (1998) find that SIEs with an independent external shear term fit the data better. They find reasonable alignments, the scatter is however larger than the one they find in Keeton et al. (1997). Gavazzi et al. (2012) find a rms scatter of 25° for the whole sample. Even after dropping the almost spherical lenses, the rms scatter is still 18° . They attribute this to a significant external shear contribution. Treu et al. (2009) even find a significant correlation between the misalignment and the local resp. global environment. In general, lenses in overdense environment seem to be more likely to be misaligned. Treu et al. (2009) and Gavazzi et al. (2012) also find a correlation with a large scatter between the ellipticities of the light and dark matter distributions.

Contrary to earlier approaches, we choose to use a non-parametric modelling technique. We use a pixel-based (see e.g. Saha & Williams (1997)) lens reconstruction framework called *GLASS* (Lubini & Coles, 2012). We apply this successfully on a sample of 15 strong gravitational lensing galaxies using stellar mass data of Leier (2011). Thus, we can disentangle dark and luminous matter and look at the shapes and alignments of these distributions. We can also look at the ellipticities of the reconstructed lenses and compare them to the ones of the stellar distribution. Furthermore, we discuss the environments of these lenses, as they might affect some properties of gravitational lenses in a significant way (Momcheva et al., 2006; Wong et al., 2011). We think that we have enough statistics to make claims about misalignments between the dark matter halo and the stellar mass distribution, and how the halo is oriented compared to the environment.

In Section 2 we present the lens sample and important properties of each lens. In Section 3 we present the

Lens	z_L	z_S	Type	Lens	z_L	z_S	Type
Q0047	0.48	3.60	Quad	PG1115	0.31	1.72	Quad
Q0142	0.49	2.72	Double	B1152	0.44	1.02	Double
MG0414	0.96	2.64	Quad	B1422	0.34	3.62	Quad
B0712	0.41	1.34	Quad	SBS1520	0.72	1.86	Double
RXJ0911	0.77	2.80	Quad	B1600	0.41	1.59	Double
BRI0952	0.63	4.50	Double	B1608	0.63	1.39	Quad
Q0957	0.36	1.41	Double	MG2016	1.01	3.27	Quad ¹
LBQS1009	0.87	2.74	Double	B2045	0.87	1.28	Quad
B1030	0.60	1.54	Double	HE2149	0.60	2.03	Double
HE1104	0.73	2.32	Double	Q2237	0.04	1.69	Quad

Table 1: List of all the lenses in the sample and their properties. Data is taken from *CASTLES* and Leier (2011). The angles are measured north-through-east.

¹ Two images merge, thus only three images can be resolved.

reconstruction method we use and our shape measure. Section 4 consists of the results of this analysis. We show the relations we find between misalignment, ellipticities, and the environment.

2 Data

The pixelated stellar mass maps we use, were reconstructed by Leier (2011). For each pixel the surface brightness was compared with stellar mass-to-light ratios, which were determined by stellar population synthesis models. This technique allows estimating the stellar mass in these pixels. Further details on this method can be found in Leier (2011), Ferreras et al. (2005), Ferreras et al. (2008).

Our sample consists of 20 galaxies. The sample is identical to the one as in Leier (2011) and Leier et al. (2011) except that *HS0818+1227* proved too difficult to reconstruct and therefore was left out. Most of the lens galaxies are early-type galaxies, except *B1030+074*, *B1152+200*, *B1600+434*, *B1608+656*, and *Q2237+030*. All lenses can also be found in the gravitational lens database *CASTLES*. Characteristics and references of each lens in the sample are listed below. Table 1 contains of all the redshifts and the type of the lenses, Table 2 lenses with environment information, and Table 3 lenses with measured time delays.

Q0047-2808 (hereafter *Q0047* or *0047*) is a luminous early-type galaxy (Warren et al., 1996). Wong et al. (2011) find a group of 9 members all of which they spectroscopically confirm.

Q0142-100 (hereafter *Q0142* or *0142*) is a passively evolving early-type galaxy according to (Lehár et al., 2000; Eigenbrod et al., 2007).

MG0414+0534 (hereafter *MG0414* or *0414*) is a passively evolving early-type galaxy (Tonry & Kochanek, 1999). Schechter & Moore (1993) find a very close luminous satellite galaxy north-west of the lens. Due to the proximity of this satellite, we include it as a point mass in our analysis.

B0712+472 (hereafter *B0712* or *0712*) is an early-type galaxy (Fassnacht & Cohen, 1998). Another galaxy, 102'' to the south-east seems to be at a similar redshift (Fassnacht & Lubin, 2002). There is also a group of 10 galaxies at a lower redshift.

RXJ0911+0551 (hereafter *RXJ0911* or *0911*) is an almost circular early-type galaxy (Sluse et al., 2012). It has measured time delays (Hjorth et al., 2002). It lies on the outskirts of a cluster (Morgan et al., 2001). This cluster seems to be rather complex and especially it is not spherical. Possibly it is not dynamically relaxed, although X-ray emission can be detected. Analysis of this emission yields a temperature of 2.3 keV. There is also a satellite galaxy to the north-west direction (Kneib et al., 2000).

BRI0952-0115 (hereafter *BRI0952* or *0952*) is an early-type galaxy (Lehár et al., 2000; Eigenbrod et al., 2007). Momcheva et al. (2006) find that the lens lies in a poor group of 5 members. However, a redshift of $z = 0.41$ was used. According to Eigenbrod et al. (2007), the redshift is more likely to be $z = 0.632$. They also find a system of 2 or 3 other galaxies at a slightly higher redshift of which the lens could be part of. The required external shear could be explained easily by a cosmic contribution (Lehár et al., 2000). Therefore, we treat this lens as an isolated object.

Q0957+561 (hereafter *Q0957* or *0957*) is a cD galaxy lying close to the center of a cluster with a high sprial galaxy-fraction (e.g. Garrett et al. (1992); Angonin-Willaime et al. (1994); Chartas et al. (1998)). Due to the

Lens	Environment ^a	Group/Cluster centroid ^b		Other galaxy		References ^c
		$\Delta\alpha$ ["]	$\Delta\delta$ ["]	$\Delta\alpha$ ["]	$\Delta\delta$ ["]	
Q0047	G(9)	3.6 ± 15.6	43.2 ± 28.8	1
MG0414	2	-0.4	1.5	2
B0712	2	47	-91	3
RXJ0911	C	-12.0	-39.8	4
Q0957	C	5
B1030	2	-9.8	8.5	6
PG1115	G(13)	-10.8 ± 21.0	-3.6 ± 15.6	1
B1422	G(17)	61.2 ± 25.2	-10.8 ± 23.4	1
SBS1520	G(5)	7
B1600	G(17)	-8.4^d	-1.5^d	8
B1608	G(8)	-0.7	8.0	9
MG2016	C(69)	10
HE2149	G	-36.6	14.2	11

Table 2: List of lenses lying in a group or cluster environment, or that have a companion.

^a G stands for group, C for cluster, and 2 means that the lens has a companion galaxy. If known, the number of member galaxies including the lens is given.

^b If not stated differently, the centroid positions are luminosity-weighted estimates.

^c References for the centroid estimates we used.

^d Only number-weighted estimates are available.

1: Wong et al. (2011); 2: Schechter & Moore (1993); 3: Fassnacht & Lubin (2002); 4: Morgan et al. (2001); 5: Chartas et al. (1998); 6: Lehár et al. (2000); 7: Auger et al. (2008); 8: Auger et al. (2007); 9: Toft et al. (2003); 10: Williams et al. (2006); 11: Williams et al. (2006)

large image separation, large physical scales are probed. As listed in Table 3 of Keeton et al. (2000), the position angles to the center of the cluster of earlier lens reconstructions range between 51.8 deg and 67.8 deg measured north-through-east. These results are consistent with the center of the X-ray emission from the cluster (Chartas et al., 1998). The lens has a measured time delay, e.g. (Shalyapin et al., 2012). They however also find a three-day lag between the g- and r-bands, and the estimates do not agree at the 2σ -level. They argue that this effect can be accounted for by the presence of a substructure and chromatic dispersion. We find that the results do not change significantly for either estimate and choose therefore the g-band measurement.

LBQS1009-0252 (hereafter *LBQS1009* or *1009*) is probably an early-type galaxy (Lehár et al., 2000). Faure et al. (2004) find no significant galaxy overdensity near the lens.

B1030+074 (hereafter *B1030* or *1030*) appears to have some substructure (Xanthopoulos et al., 1998). Lehár et al. (2000) conclude that there are two distinct galaxies. The main one is a red, early-type galaxy. The other component seems to be fitted well by an exponential disk galaxy. They also conclude that no firm statements about the environment can be made. Although there is another galaxy nearby, it is too blue to be an early-type galaxy and thus they cannot estimate its shear contribution.

HE1104-1805 (hereafter *HE1104* or *1104*) is probably an early-type galaxy (Lehár et al., 2000; Courbin et al., 2000). It has measured time delays (Morgan et al., 2008). Lehár et al. (2000) also seem to find a group environment. Faure et al. (2004) however conclude that the photometric redshift measurements of these galaxies indicate that they are at a higher redshift and rather associated with the source. Nonetheless, their lens models, parametric and free-form, all require strong external shear.

PG1115+080 (hereafter *PG1115* or *1115*) is an early-type galaxy (Yoo et al., 2005). It has measured time delays. We use recent estimates of the time delays by Tsvetkova et al. (2010) which differ significantly from traditional values by e.g. Barkana (1997). Momcheva et al. (2006) and Wong et al. (2011) analyzed the environment of the lens thoroughly. It is part of a small group of 13 members. Grant et al. (2004) detect also X-ray emission from the corresponding group, which yields a temperature of 0.8 keV.

B1152+200 (hereafter *B1152* or *1152*) seems to have a color consistent with a late-type or an irregular galaxy (Toft et al., 2000). Not much seems to be known about the environment of the lens.

B1422+231 (hereafter *B1422* or *1422*) is an early-type galaxy (Impey et al., 1996). Although there are measured time delays by Patnaik & Narasimha (2001), they are probably not to be trusted too much as they deviate significantly from theoretical expectations in Raychaudhury et al. (2003). An accurate measurement of the time delays would require time delay measurements on the scale of hours. Momcheva et al. (2006) find a group en-

Lens		Time delays [d]			References
RXJ0911	$\Delta t_{BA} = 146 \pm 4$	1
Q0957	$\Delta t_{BA} = 416.5 \pm 1.0^a$	$\Delta t_{BA} = 420.6 \pm 1.9^b$	2
HE1104	$\Delta t_{BA} = 162.2^{+6.3}_{-5.9}$	3
PG1115	$\Delta t_{BA} = 12.0^{+2.4}_{-2.0}$	$\Delta t_{DC} = 4.4^{+3.2}_{-2.4}$	4
SBS1520	$\Delta t_{BA} = 125.8 \pm 2.1$	5
B1600	$\Delta t_{BA} = 51 \pm 2$	6
B1608	$\Delta t_{BA} = 31.5^{+2}_{-1}$	$\Delta t_{CA} = 36.0 \pm 1.5$	$\Delta t_{DA} = 77.0^{+2}_{-1}$...	7
HE2149	$\Delta t_{BA} = 103 \pm 12$	8

Table 3: Lenses with measured time delays. Δt_{BA} corresponds to the time delay between the images A and B with A leading.

^a measured in the g-band

^b measured in the r-band

1: Hjorth et al. (2002); 2: Shalyapin et al. (2012); 3: Morgan et al. (2008); 4: Tsvetkova et al. (2010); 5: Eulaers & Magain (2011); 6: Burud et al. (2000); 7: Fassnacht et al. (2002); 8: Burud et al. (2002a)

vironment with 16 spectroscopically confirmed member galaxies. Using newer data, Wong et al. (2011) find an additional member. Grant et al. (2004) also detect X-ray emission from the corresponding group at a temperature of 1.0 keV.

SBS1520+530 (hereafter *SBS1520* or *1520*) is an early-type galaxy, possibly with a disc (Auger et al., 2008). It has measured time delays (Eulaers & Magain, 2011). There is some uncertainty about the redshift of the galaxy. Burud et al. (2002b) find that their spectroscopic redshift estimate is consistent with $z = 0.71$, which was measured first by Chavushyan et al. (1997). Both however also find a system at $z = 0.82$, which could be the main lens. Burud et al. (2002b) however conclude that it is not associated with the lens. Auger et al. (2008) argue that a system they find at $z = 0.76$ is more likely to be the lens, and the foreground system at $z = 0.71$ is just a local perturber. Data seems however not conclusive. Auger et al. (2008) find and spectroscopically confirm a total of 3 groups along the line of sight. A poor group of 5 members is at $z = 0.716$, another one with 13 members is at $z = 0.758$, and a third group with 10 members is at a higher redshift $z = 0.818$.

B1600+434 (hereafter *B1600* or *1600*) is a nearly edge-on viewed late-type galaxy (Jaunsen & Hjorth, 1997). The lens lies in a group with at least seven members, which all seem to be late-type galaxies (Auger et al., 2007).

B1608+656 (hereafter *B1608* or *1608*) consists of two merging galaxies. The main galaxy is an early-type galaxy which is disrupted by a smaller, probably late-type galaxy (Surpi & Blandford, 2003). The system has measured time delays (Fassnacht et al., 2002). The environment and the mass distribution along the line of sight have been analyzed by Fassnacht et al. (2006). They find a group with 8 resp. 9 members if the merging galaxies are counted as 2. No significant X-ray emission was detected from the surrounding group (Dai & Kochanek, 2005). Along the line of sight seem to be four other groups.

MG2016+112 (hereafter *MG2016* or *2016*) is a giant elliptical galaxy (Lawrence et al., 1984; Schneider et al., 1986). It is the farthest lens we consider in this sample. It lies in a cluster which consists of 69 probable galaxies (Toft et al., 2003). The clusters shows a high density of galaxies close to the lens in a south-east direction.

B2045+265 (hereafter *B2045* or *2045*) is probably an elliptical galaxy (McKean et al., 2007). Fassnacht et al. (1999) initially classified the galaxy as a late-type Sa galaxy, the velocity dispersion however seems too high. As the source redshift is rather low, a large lens mass is needed. McKean et al. (2007) therefore conclude that it is more likely an elliptical galaxy. To the west of the lens, Fassnacht et al. (1999) find that a group at a similar redshift as the lens. McKean et al. (2007) also find evidence for a dwarf satellite galaxy. As the measurements are not conclusive, we chose to treat the lens as an isolated object.

HE2149-2745 (hereafter *HE2149* or *2149*) is an early-type galaxy (Eigenbrod et al., 2007). It has a measured time delay (Burud et al., 2002a). There is some uncertainty in estimating the lens' redshift. Initial estimates by Wisotzki et al. (1996); Kochanek et al. (2000) found a probable redshift range of $\sim 0.2 - 0.5$. By cross-correlating the lens spectrum with a template spectrum of an elliptical galaxy, Burud et al. (2002a) find that the redshift probably lies in the range $0.49 \leq z \leq 0.60$, with the most likely redshift $z = 0.495 \pm 0.01$. Eigenbrod et al. (2007) however find that the redshift is more likely to be $z = 0.603 \pm 0.001$. This would probably make the lens part of a poor group found by Momcheva et al. (2006) and Williams et al. (2006). They also find two other groups at lower redshifts.

Q2237+030 (hereafter *Q2237* or *2237*) is a barred spiral (Yee, 1988). With only a redshift of $z = 0.04$, it is the closest lens of the sample. Due to the low redshift, the probed physical scales are quite small. No further inquiries into the environment were made.

Further information about the sample can be found in Leier (2011), Leier et al. (2011), and Sluse et al. (2012).

3 Method

3.1 GLASS

We use the new free-form lens modelling framework *GLASS* (Lubini & Coles, 2012). As its predecessor *PixeLens* (Saha & Williams, 2004), it generates a pixelated mass map of a lens reproducing the image positions perfectly. Using pixels the arrival time surface for a source at position θ_S , taking the geometric and Shapiro contributions into account, can be expressed in terms of the surface mass density κ_n of the n-th pixel rescaled by the critical density Σ_{crit} and the contribution to the gravitational potential by this pixel ψ_n (Saha & Williams, 1997)

$$\tau(\boldsymbol{\theta}) = \frac{1}{2}|\boldsymbol{\theta}|^2 - \boldsymbol{\theta} \cdot \boldsymbol{\theta}_S - \sum_n \kappa_n \psi_n(\boldsymbol{\theta}). \quad (1)$$

According to Fermat's principle, lensed images appear where the arrival time surface takes on extremal values $\nabla\tau(\boldsymbol{\theta}) = 0$. Thus, the image positions fulfil

$$\boldsymbol{\theta} - \boldsymbol{\theta}_S - \sum_n \kappa_n \alpha_n = 0, \quad (2)$$

where α_n is the contribution to the bending angle of the n-th pixel. For pixels, α_n and also ψ_n can be described by analytic formulae (Saha & Williams, 1997). Reconstructing the lens, i.e. describing the surface mass density in every pixel, reduces thus to finding sets of 'coefficients' $\{\kappa_n\}$ of these functions. As the number of pixels sets the resolution, this problem is however highly underconstrained. The number of pixels is typically $\gtrsim 100$. The solution to this is noticing that the equation is linear in κ_n . Additional constraints on the lens such as individual time delays between images and their order and all the priors we impose are also linear. The solution space is thus a high-dimensional polytope.

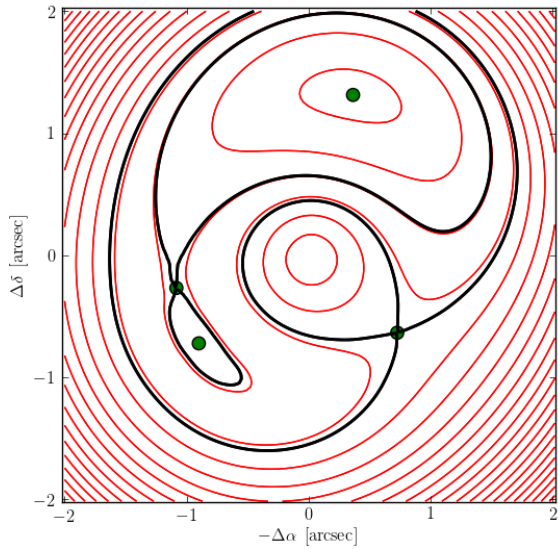
A difficulty in mass modelling is the nonuniqueness of solutions. They are not only not unique, every configuration which fulfils the equation is also equally probable. Therefore, this polytope needs to be sampled in a uniform way to analyze the full range of solutions. Due to the high dimensionality, sophisticated sampling methods of such volumes are required. Here *GLASS* and *PixeLens* differ in the method they use. Coles (2008) and Lubini & Coles (2012) show that *PixeLens* does not produce uncorrelated random samples. They propose a new sampling algorithm. They prove that generic high-dimensional polytopes indeed are sampled in a much more uniform way. Models in *GLASS* are generated using a MCMC-method with a Metropolis-Hastings algorithm. A new step x_{i+1} of the Markov chain is accepted with the probability

$$\alpha = \min \left(1, \frac{P(x_{i+1})Q(x_i, x_{i+1})}{P(x_i)Q(x_{i+1}, x_i)} \right), \quad (3)$$

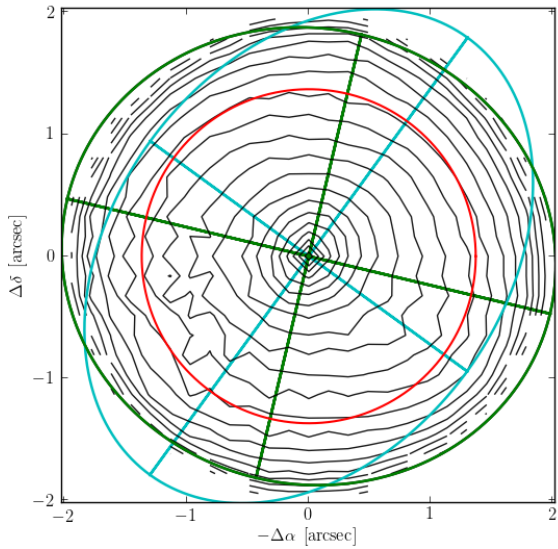
where $P(x)$ is the probability distribution samples are drawn from, and $Q(x_i, x_{i+1})$ is the proposal density. It is special in mass modelling that all the valid mass configurations have the same probability, thus P is a constant $\equiv 1$. For Markov chains Q has to be symmetric. It is usually taken to be a multivariate Gaussian $\mathcal{N}(x, \hat{\Sigma})$, where $\hat{\Sigma}$ is an estimate of the true covariance matrix Σ . In principle it could be estimated by an adaptive chain during the random walk, but then the chain is no longer Markovian as it loses the reversibility property. Therefore, first an initial adaptive burn-in phase is run to get a good estimate $\hat{\Sigma}$, before the real MCMC random walk. Many models can thus be generated and the solution space sampled. The estimation of the covariance matrix is refined in *GLASS* such that models are much less correlated. Further details and tests of the method can be found in Lubini & Coles (2012).

3.2 Priors and assumptions

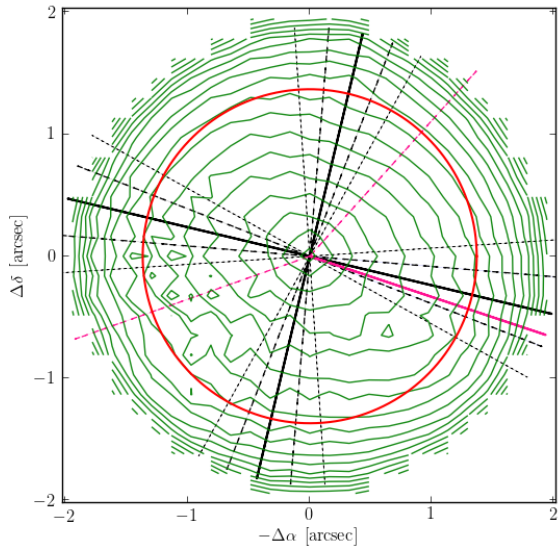
We use different priors and assumptions to eliminate unphysical mass reconstructions of the lens. First of all, the densities κ_n need to be always positive. The density must always increase towards the center, why we chose to require the local density gradient in every pixel except the central one to point within an angle of 50° towards the center. Also, the radial density profile has to decrease monotonically.



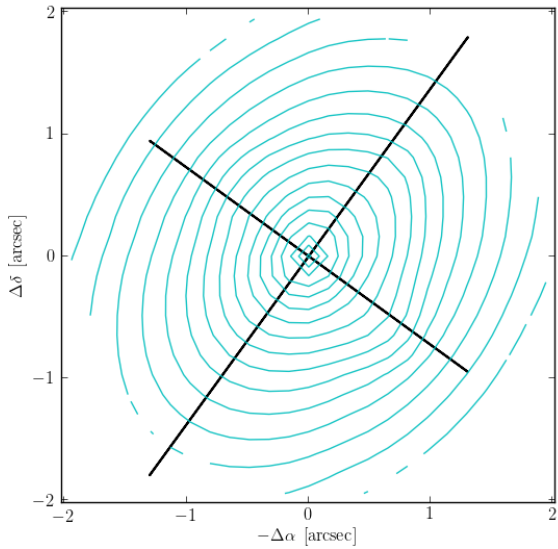
(a)



(b)



(c)



(d)

Figure 1: Reconstruction of lens *PG1115*. The plots show the mean model of the generated ensemble of models. The coordinate system is centered on the lens galaxy. (a) shows the arrival time surface. The green dots are the images, the red curves are isochrones, and the black curve are the lemniscate resp. the limaçon. (b) shows the total matter distribution. The red circle marks the circle of the outermost image. The green resp. cyan ellipses mark the shape of the dark matter resp. stellar distribution. This shape is measured as described in Section 3.3. In this case, the shape of the total matter distribution (black) is indistinguishable from the dark matter distribution. (c) shows the dark matter distribution. The black lines show the median semi-major resp. semi-minor axis with 1σ - and 2σ -uncertainties. The solid pink line points to the group centroid with 1σ -uncertainties (dashed). (d) shows the luminous matter distribution.

To avoid large fluctuations in the density, we choose to add a smoothing prior. The density in any pixel except the central one is at most twice the average density of its neighboring pixels. If there is reason to expect an invariant

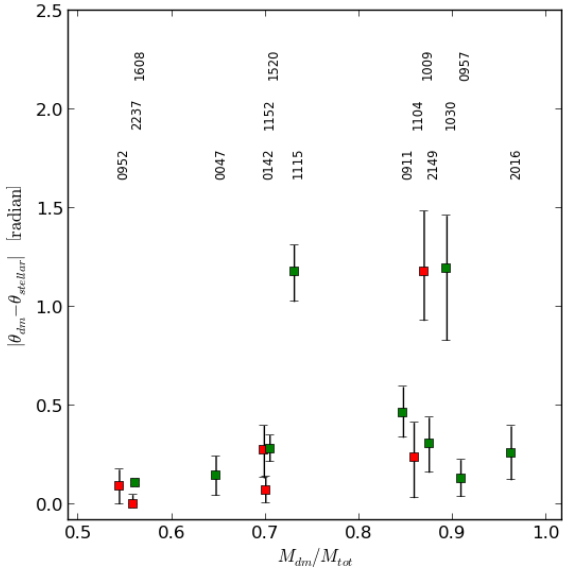


Figure 2: Misalignment between stellar and dark matter distributions versus the ratio of dark matter mass and total mass included in the radius of the outermost image. As these angles are π -periodic, the absolute value of the difference ranges from 0 to $\frac{\pi}{2}$. Green squares are the lenses inside a group/cluster or that have a companion, red squares are without.

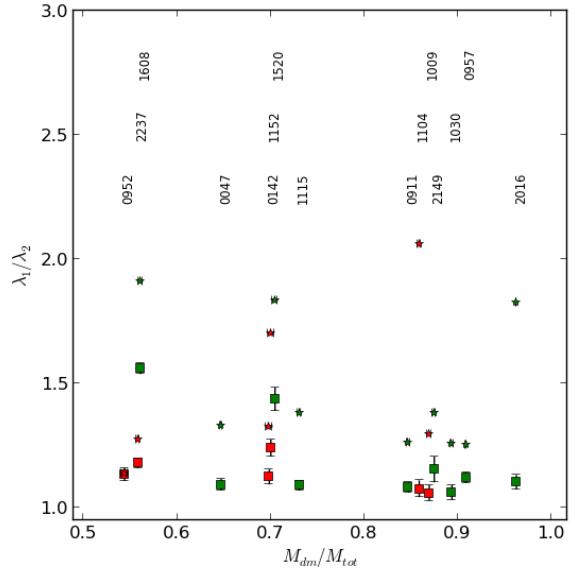


Figure 3: Ellipticities of the stellar (stars) and dark matter (squares) distributions versus the ratio of dark matter mass and total mass included in the radius of the outermost image. Green squares are the lenses inside a group/cluster or that have a companion, red squares are without.

distribution under a rotation by 180° (e.g. for doubles), we impose such a symmetry prior.

We also choose to include external shear. Thus, there is an additional term

$$\gamma_1 (\theta_x^2 - \theta_y^2) + 2\gamma_2 \theta_x \theta_y \quad (4)$$

in (1) and the subsequent equations. We allow γ_1 and γ_2 to vary, while fixing the maximum absolute value of the shear parameters. For doubles we fix the absolute value to be at most 10^{-2} (resp. 10^{-1} if no model could be generated for lower values).

We further assume that we know the positions of the images and the lens perfectly. As the range of possible models is much larger than the errors on these quantities (Saha et al., 2006), this assumption is justified. We also fix a time order of the images. Furthermore, we chose a flat concordance cosmology with $\Omega_m = 0.28$, $\Omega_\Lambda = 0.72$, and $H_0^{-1} = 13.7$.

3.3 Shape measure

To get a rough estimate of the shape of the surface mass distribution we use the inverse of the moment of inertia tensor of the mass map. Its eigenvectors and eigenvalues track the shape of the mass distribution. There are thus two quantities which define the shape, the ratio of the eigenvalues λ_1/λ_2 , which describes the ellipticity, and the angle of the semi-major axis θ . This seemingly crude measure was tested on fake data and found to be working well.

Figure 1 shows example plots of the reconstruction of the lens PG1115. They illustrate this shape measure. In this case, there is a significant misalignment between the two mass distributions. Also the uncertainties on the angle estimate are shown. Errors are purely statistical. Figure 1 also shows the arrival time surface and total, dark, and baryonic mass distributions.

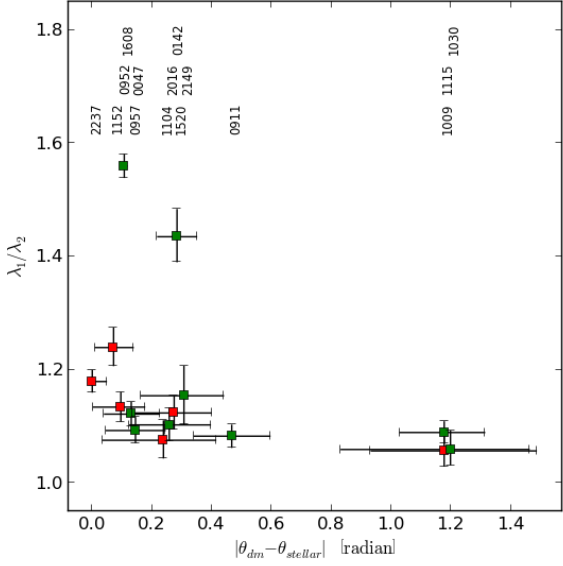


Figure 4: Misalignment between stellar and dark matter distributions versus the ellipticity of the dark matter halo. As these angles are π -periodic, the absolute value of the difference ranges from 0 to $\frac{\pi}{2}$. Green squares are the lenses inside a group/cluster or that have a companion, red squares are without.

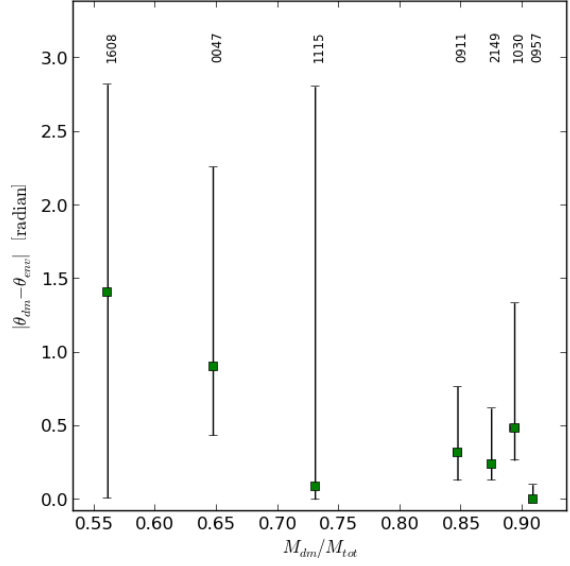


Figure 5: Misalignment between the dark matter halo of lenses with known environment and the direction of the centroid resp. the companion galaxy versus the ratio of dark matter mass and total mass included in the radius of the outermost image. Although the angle of the semi-major axis is π -periodic, the direction of the centroid position is not. The absolute value of the difference ranges therefore from 0 to π .

4 Results

4.1 Lens Reconstruction

As it was not possible to reconstruct some lenses, we had to drop the lenses *MG0414*, *B0712*, *B1422*, *B1600*, *B2045*. They will however be included in a future paper. The sample thus includes a total of 15 gravitational lenses. For every lens a total number of 10000 models were generated. This number we've chosen gives reasonable statistics, while not being computationally too expensive.

In general an external shear of $|\gamma_i| \lesssim 10^{-1}$ is required to model the lenses. *RXJ0911*, *B1608*, and *MG2016* however need a significantly larger external shear of $|\gamma_i| \sim 2 \cdot 10^{-1}$. This probably can be attributed to the cluster environment resp. the merging process in the system *B1608*, which makes it hard to model. Furthermore, an external shear of at most $|\gamma_i| \lesssim 10^{-1}$ is needed to be assumed to model *SBS1520*.

The masses M_{dm} and $M_{tot} = M_{dm} + M_{stellar}$ we define in this analysis, are always the mass included up to the radius of the outermost image. Our mass modelling shows that *BRI0952*, *B1608*, and *Q2237* seem to have a significant amount of the total mass in baryonic mass. This can be explained for *Q2237* and *B1608*. Due to the galaxy merger, the outermost image for the lens *B1608* includes mainly the central parts of the two galaxies. In *Q2237* only the inner parts of the lens, where the baryonic mass dominates, are probed. Also the two very massive, very dark matter dominated lenses *Q0957* and *MG2016* should be mentioned. *Q0957* is a cD-galaxy and *MG2016* a giant elliptical, so this result was to be expected.

Surprisingly, the shape measure we define yields results that are constrained quite well, as can be seen in Figures 1, 6-21. The errors, which are purely statistical, on the ellipticities and the angles of the semi-major axis do not dominate the result. Lenses with almost spherical halos, i.e. $\lambda_1/\lambda_2 \sim 1$, should however be treated with caution.

As mentioned in Section 2, there are different time delay estimates for *PG1115*. We find that the results do not change much when changing the time delays. As can be seen in Figure 1 resp. Figure 14 and Figure 15, the dark matter distribution is a bit more spherical with the time delays from Tsvetkova et al. (2010) and the uncertainty on the angle of the semi-major axis grows. The misalignment we see is thus not affected by different time delays.

The dark matter distribution in *SBS1520* shows a very interesting behaviour. As can be seen in Figure 17, the dark matter seems to follow the baryonic mass distribution. Further out however, the dark matter distribution is rotated slightly. There is a significant misalignment between the dark matter distribution and the baryonic distribution. Without the central part, the misalignment would be even larger. This behaviour could be due to the potential disc Auger et al. (2008), or caused by the many structures on the line of sight.

4.2 Misalignments between stellar and dark matter distributions

Figure 2 shows the differences between the angles of the stellar and the dark matter semi-major axes versus the ratio of the included dark matter and total mass. For lenses with a significant stellar component inside the outermost image radius, the distributions seem to be rather aligned. It seems that if the luminous mass is comparable to the dark matter mass, then the distributions align. For a smaller stellar contribution this is not necessarily the case. The scatter increases and there can be significant misalignments, which can be seen especially clearly in the systems *PG1115* (Figures 1 or 14) and *RXJ0911* (Figure 8). While alignments between the distributions are preferred, they do not seem to be a necessary condition.

The environment might also play a role. Red are the systems, which are isolated or no group resp. cluster environment has been found, green the ones in such an environment. The misaligned systems are mainly the lenses with a known environment. Therefore, this misalignment could be caused by the external effects.

4.3 Ellipticities of stellar and dark matter distributions

The ellipticities of the distributions versus the mass ratio are shown in Figure 3. We see, that every dark matter halo has a lower ellipticity λ_1/λ_2 and is thus closer to sphericity than the luminous galaxy. The systems *HE1104* (Figure 13) and *MG2016* (Figure 19) show especially large differences. It is not clear what could cause these

Figure 4 shows the misalignment versus the ellipticity of the dark matter halo. There seem to be five different regions. Almost spherical halos with good alignment of the semi-major axes, almost spherical halos with good alignment of semi-major and semi-minor axes (maximum misalignment between the semi-major axes), more elliptical, aligned halos, a seemingly ‘forbidden’ region for misalignments in between, and the upper right triangle, i.e. larger ellipticities and misalignments, which also seems forbidden. Understanding Figure 4 is certainly not trivial. Alignment with the semi-minor axis might be a stable configuration for almost spherical halos, while slightly smaller misalignments are unstable. There also seem to be some outliers as *PG1115*, *SBS1520*, and *HE2149*.

4.4 Misalignments between the dark matter distributions and environment

Figure 5 shows the misalignment between the direction to the group or cluster centroid resp. the companion galaxy with the dark matter halo. Although the error bars are huge, we immediately see that three lenses are basically aligned with the environment. The four other systems show slight misalignment. Having a closer look at these lenses shows however that at least two of them might in fact be aligned. For *RXJ0911* and *HE2149* there are no errors on the estimates of the centroid. Otherwise they would probably agree very well. *Q0047* does not seem to be aligned with the direction of the group centroid. This could be due to the fact that the lens itself is quite far away from the centroid. The halo of *B1030* is almost spherical, so the apparent misalignment could maybe be explained. It is also the only lens with only one companion galaxy. It is possible that in this case the effect of the environment is not strong enough. We however certainly lack data to make any claims for the systems with just one companion galaxy. Then, there is also *MG2016*, which is not shown here, as the centroid was not measured in this cluster. There is however a high galaxy density towards the south-east, where also the cluster centroid probably lies. Judging from Figure 19, the halo seems to be aligned with the cluster centroid.

We conclude that lenses in groups or cluster are maybe aligned with the centroid. However, as we lack the statistics and as the errors on the centroid positions are huge, this claim might be disproved. It is not possible at this point to make a similar statement for lenses with just one companion galaxy.

5 Conclusion

We used a nonparametric modelling method to reconstruct a total of 15 lenses. Using previously measured light maps, then converted to luminous mass maps Leier (2011), we were able to isolate the dark matter distribution. We used the eigenvalues and eigenvectors of the inverse of the moment of inertia tensor to characterize the shape of the light and mass distributions. This allowed us to analyze the alignment between these distributions and the relation between the ellipticities. Furthermore, we included environment information, which we related to the misalignment.

Our results can be summarized in the following way. If lenses lie in dense environments, mass and light need not be aligned. This might also be the case for lenses without known environments. We found more scatter than previous analyses by Keeton et al. (1997), Koopmans et al. (2006), Treu et al. (2009), and Gavazzi et al. (2012) which all used SIEs mostly neglecting external shear to model the lenses. We also found that the semi-major and semi-minor axes of the distributions can be aligned, if the dark matter halos are close to sphericity. Up to our knowledge, this result was not obtained in other analyses.

We found that dark matter halos are rounder than the luminous galaxies, i.e. they have a lower eigenvalue ratio λ_1/λ_2 . Previous analyses found a correlation between the ellipticities (Treu et al., 2009; Gavazzi et al., 2012), which we do not see. They also found a couple of cases, where the stellar distribution is more spherical than the dark matter halo. We claim that certain combinations of ellipticity of the dark matter halo and misalignment between light and mass seem to be forbidden. However, more lens systems are needed to support this claim.

We suspect that the dark matter halo might be aligned with the centroid of the group or cluster it lies in. Due to the large uncertainties in the centroid positions however, such alignments might as well be coincidences.

We want to stress again that the systems *SBS1520* and *PG1115*, which both show some misalignment and have time delay measurements, seem interesting enough to investigate further. In *SBS1520* we found that the outer parts of the dark matter distribution is rotated respective to the central, which displays an interesting feature possibly due a disc. It is on the other hand a very complicated system with a lot of structures along the line of sight. *PG1115* is easy to model, but still shows a clear misalignment. Thus, it could serve as a test for other methods that try to reproduce these misalignments.

REFERENCES

- Angonin-Willaime M.-C., Soucail G., Vanderriest C., 1994, A&A, 291, 411
 Auger M. W., Fassnacht C. D., Abrahamse A. L., Lubin L. M., Squires G. K., 2007, AJ, 134, 668
 Auger M. W., Fassnacht C. D., Wong K. C., Thompson D., Matthews K., Soifer B. T., 2008, ApJ, 673, 778
 Barkana R., 1997, ApJ, 489, 21
 Burud I., Courbin F., Magain P., et al., 2002a, A&A, 383, 71
 Burud I., Hjorth J., Courbin F., et al., 2002b, A&A, 391, 481
 Burud I., Hjorth J., Jaunsen A. O., et al., 2000, ApJ, 544, 117
 Chartas G., Chuss D., Forman W., Jones C., Shapiro I., 1998, ApJ, 504, 661
 Chavushyan V. H., Vlasyuk V. V., Stepanian J. A., Erastova L. K., 1997, A&A, 318, L67
 Coe D., Fuselier E., Benítez N., Broadhurst T., Frye B., Ford H., 2008, ApJ, 681, 814
 Coles J., 2008, ApJ, 679, 17
 Courbin F., Lidman C., Meylan G., Kneib J.-P., Magain P., 2000, A&A, 360, 853
 Dai X., Kochanek C. S., 2005, ApJ, 625, 633
 Eigenbrod A., Courbin F., Meylan G., 2007, A&A, 465, 51
 Eulaers E., Magain P., 2011, A&A, 536, A44
 Fassnacht C. D., Blandford R. D., Cohen J. G., et al., 1999, AJ, 117, 658
 Fassnacht C. D., Cohen J. G., 1998, AJ, 115, 377
 Fassnacht C. D., Gal R. R., Lubin L. M., McKean J. P., Squires G. K., Readhead A. C. S., 2006, ApJ, 642, 30
 Fassnacht C. D., Lubin L. M., 2002, AJ, 123, 627
 Fassnacht C. D., Xanthopoulos E., Koopmans L. V. E., Rusin D., 2002, ApJ, 581, 823
 Faure C., Alloin D., Kneib J. P., Courbin F., 2004, A&A, 428, 741
 Ferreras I., Saha P., Burles S., 2008, MNRAS, 383, 857
 Ferreras I., Saha P., Williams L. L. R., 2005, ApJL, 623, L5
 Garrett M. A., Walsh D., Carswell R. F., 1992, MNRAS, 254, 27P
 Gavazzi R., Treu T., Marshall P. J., Brault F., Ruff A., 2012, ApJ, 761, 170
 Grant C. E., Bautz M. W., Chartas G., Garmire G. P., 2004, ApJ, 610, 686
 Hjorth J., Burud I., Jaunsen A. O., et al., 2002, ApJL, 572, L11
 Impey C. D., Foltz C. B., Petry C. E., Browne I. W. A., Patnaik A. R., 1996, ApJL, 462, L53
 Jaunsen A. O., Hjorth J., 1997, A&A, 317, L39

- Keeton C. R., Falco E. E., Impey C. D., et al., 2000, ApJ, 542, 74
- Keeton C. R., Kochanek C. S., Falco E. E., 1998, ApJ, 509, 561
- Keeton C. R., Kochanek C. S., Seljak U., 1997, ApJ, 482, 604
- Kneib J.-P., Cohen J. G., Hjorth J., 2000, ApJL, 544, L35
- Kochanek C. S., Falco E. E., Impey C. D., et al., 2000, ApJ, 543, 131
- Koopmans L. V. E., Treu T., Bolton A. S., Burles S., Moustakas L. A., 2006, ApJ, 649, 599
- Kormann R., Schneider P., Bartelmann M., 1994, A&A, 284, 285
- Lawrence C. R., Schneider D. P., Schmidt M., et al., 1984, Science, 223, 46
- Lehár J., Falco E. E., Kochanek C. S., et al., 2000, ApJ, 536, 584
- Leier D., 2011, On the Distribution of Luminous and Dark Matter in Strong Lensing Galaxies, Ph.D. thesis, Astronomisches Rechen-Institut, Zentrum für Astronomie der Universität Heidelberg
- Leier D., Ferreras I., Saha P., Falco E. E., 2011, ApJ, 740, 97
- Lubini M., Coles J., 2012, MNRAS, 425, 3077
- McKean J. P., Koopmans L. V. E., Flack C. E., et al., 2007, MNRAS, 378, 109
- Momcheva I., Williams K., Keeton C., Zabludoff A., 2006, ApJ, 641, 169
- Morgan C. W., Eyler M. E., Kochanek C. S., et al., 2008, ApJ, 676, 80
- Morgan N. D., Chartas G., Malm M., et al., 2001, ApJ, 555, 1
- Patnaik A. R., Narasimha D., 2001, MNRAS, 326, 1403
- Raychaudhury S., Saha P., Williams L. L. R., 2003, AJ, 126, 29
- Saha P., Coles J., Macciò A. V., Williams L. L. R., 2006, ApJL, 650, L17
- Saha P., Williams L. L. R., 1997, MNRAS, 292, 148
- Saha P., Williams L. L. R., 2004, AJ, 127, 2604
- Schechter P. L., Moore C. B., 1993, AJ, 105, 1
- Schneider D. P., Gunn J. E., Turner E. L., et al., 1986, AJ, 91, 991
- Shalyapin V. N., Goicoechea L. J., Gil-Merino R., 2012, A&A, 540, A132
- Sluse D., Chantry V., Magain P., Courbin F., Meylan G., 2012, A&A, 538, A99
- Surpi G., Blandford R. D., 2003, ApJ, 584, 100
- Toft S., Hjorth J., Burud I., 2000, A&A, 357, 115
- Toft S., Soucail G., Hjorth J., 2003, MNRAS, 344, 337
- Tonry J. L., Kochanek C. S., 1999, AJ, 117, 2034
- Treu T., Gavazzi R., Gorecki A., et al., 2009, ApJ, 690, 670
- Tsvetkova V. S., Vakulik V. G., Shulga V. M., et al., 2010, MNRAS, 406, 2764
- Warren S. J., Hewett P. C., Lewis G. F., Moller P., Iovino A., Shaver P. A., 1996, MNRAS, 278, 139
- Williams K. A., Momcheva I., Keeton C. R., Zabludoff A. I., Lehár J., 2006, ApJ, 646, 85
- Wisotzki L., Koehler T., Lopez S., Reimers D., 1996, A&A, 315, L405
- Wong K. C., Keeton C. R., Williams K. A., Momcheva I. G., Zabludoff A. I., 2011, ApJ, 726, 84
- Xanthopoulos E., Browne I. W. A., King L. J., et al., 1998, MNRAS, 300, 649
- Yee H. K. C., 1988, AJ, 95, 1331
- Yoo J., Kochanek C. S., Falco E. E., McLeod B. A., 2005, ApJ, 626, 51

A Reconstructed Lenses

The reconstructions that were used in the analysis are shown in Figures 6-21

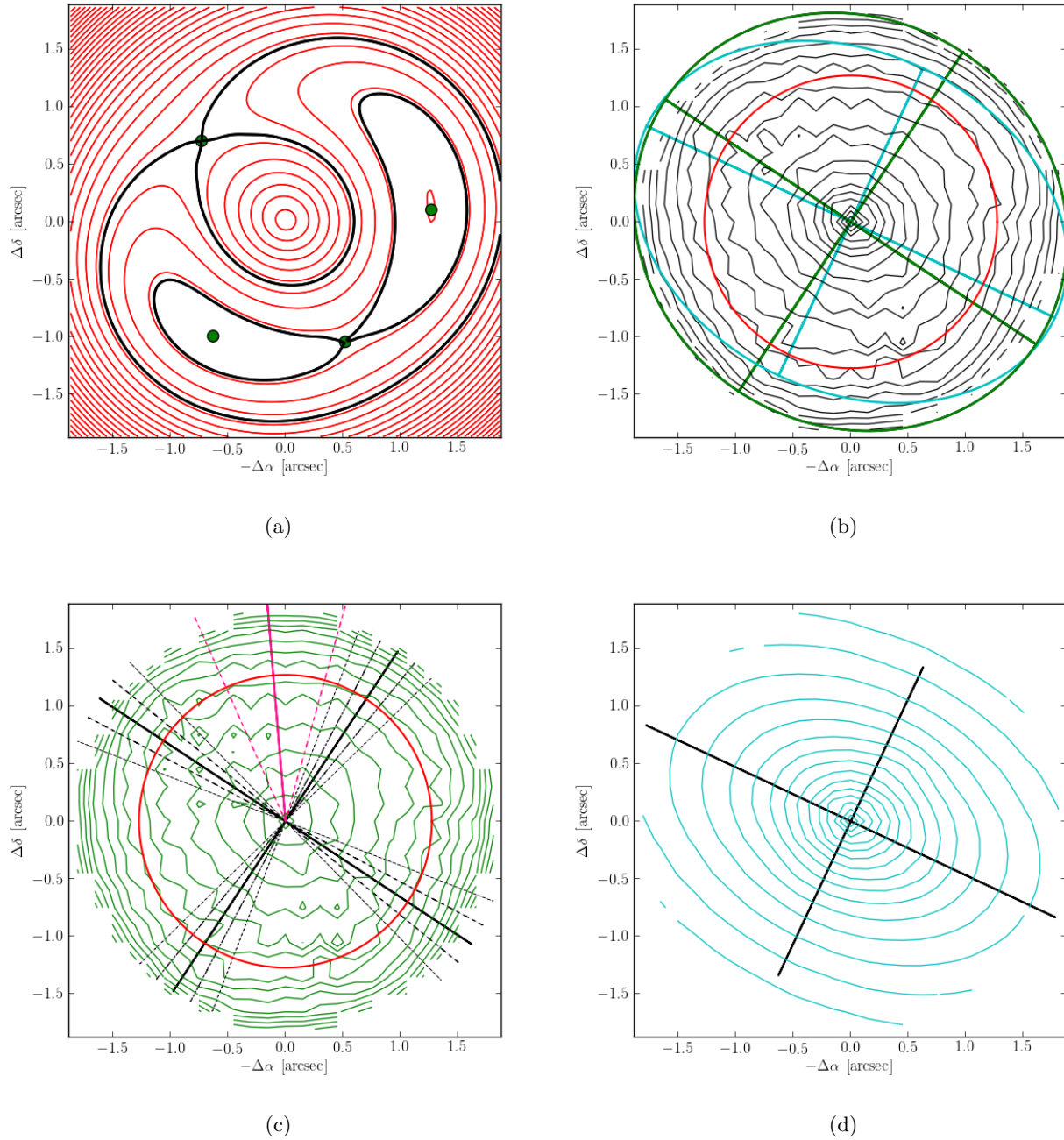
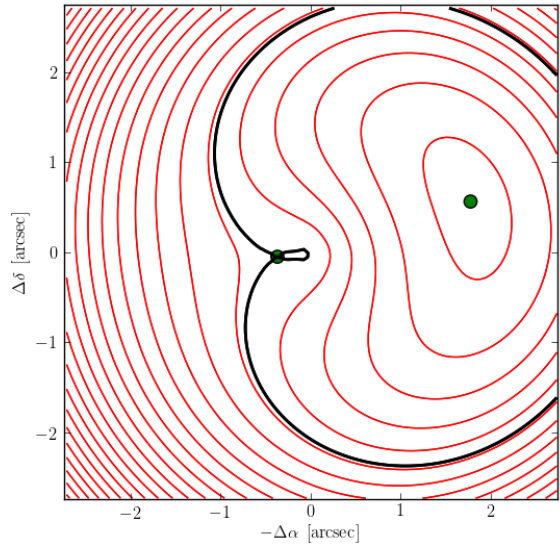
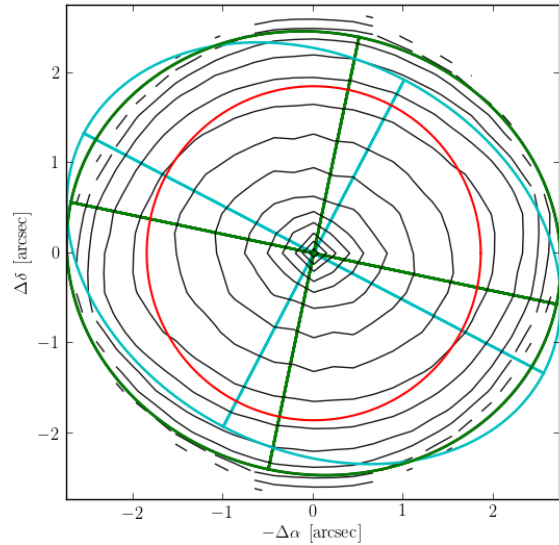


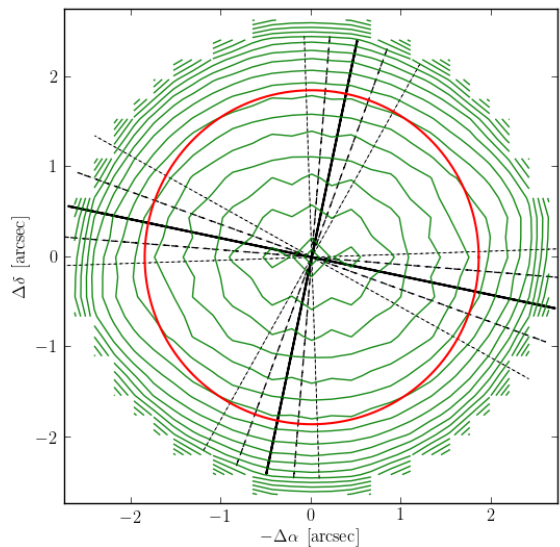
Figure 6: Reconstruction of lens *Q0047*. Analogous to Figure 1.



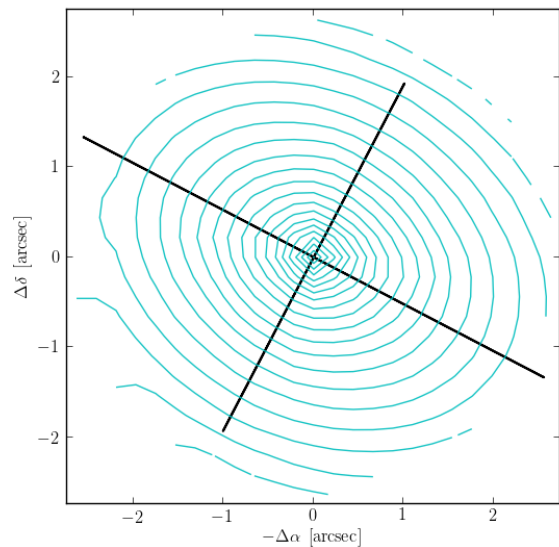
(a)



(b)

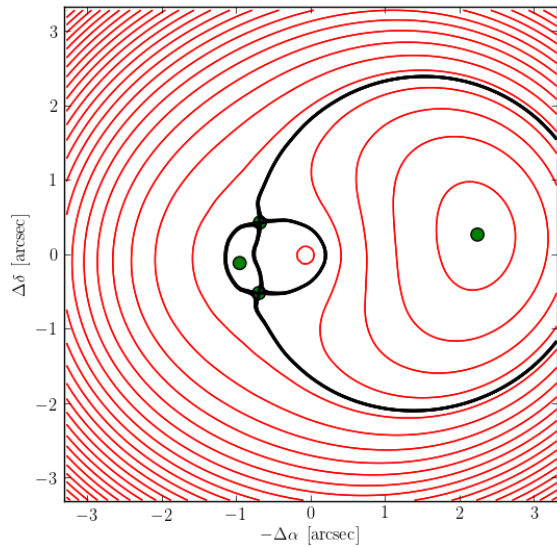


(c)

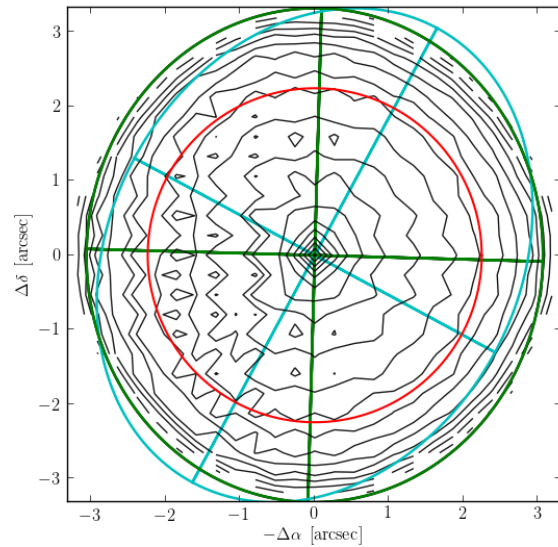


(d)

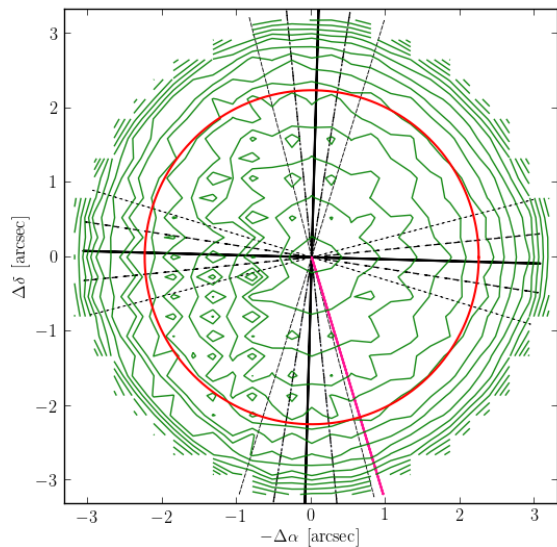
Figure 7: Reconstruction of lens $Q0142$. Analogous to Figure 1.



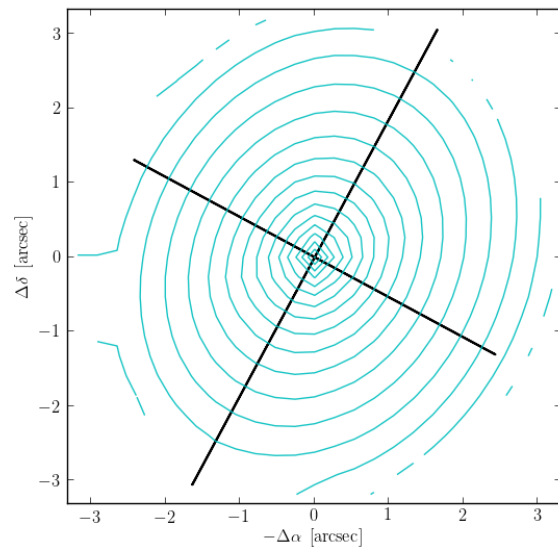
(a)



(b)

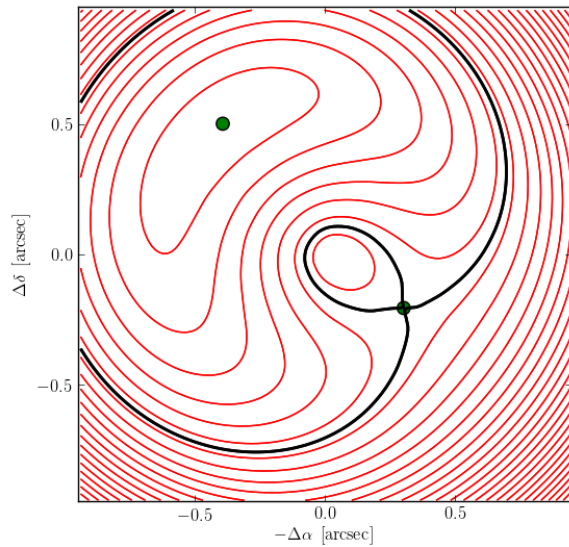


(c)

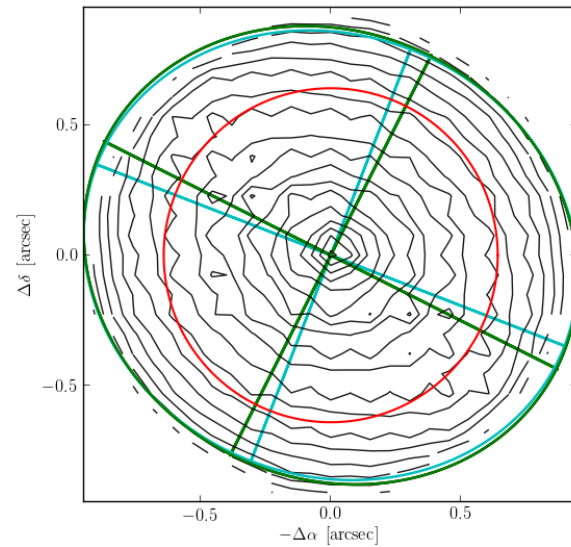


(d)

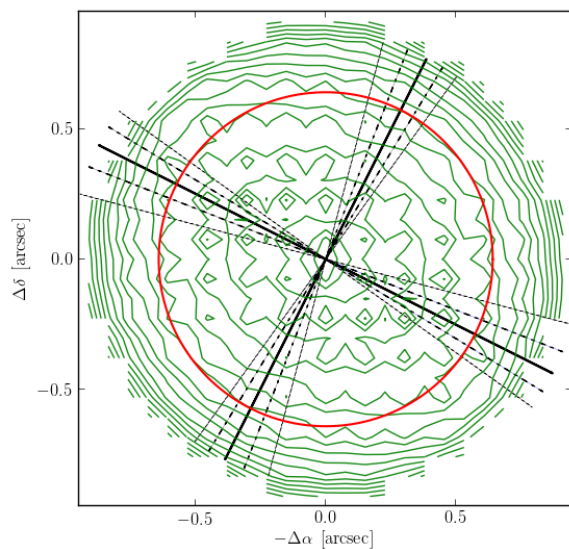
Figure 8: Reconstruction of lens *RXJ0911*. Analogous to Figure 1.



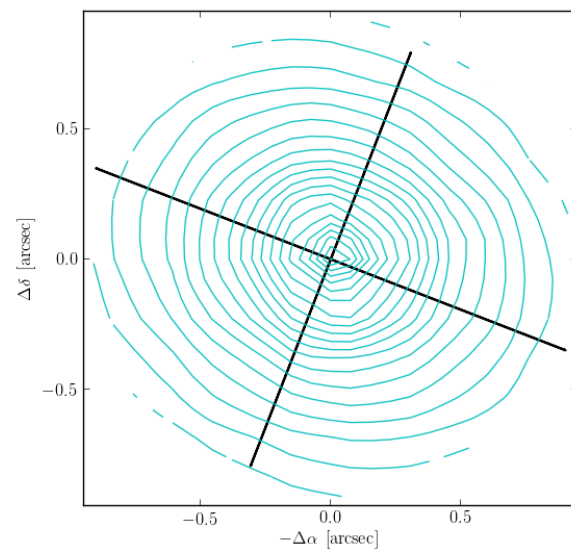
(a)



(b)

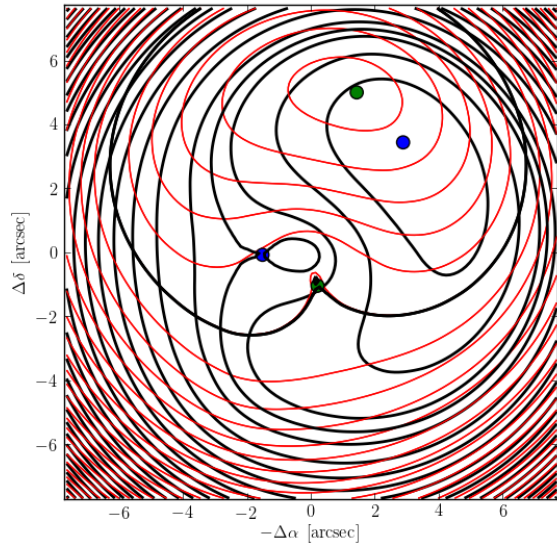


(c)

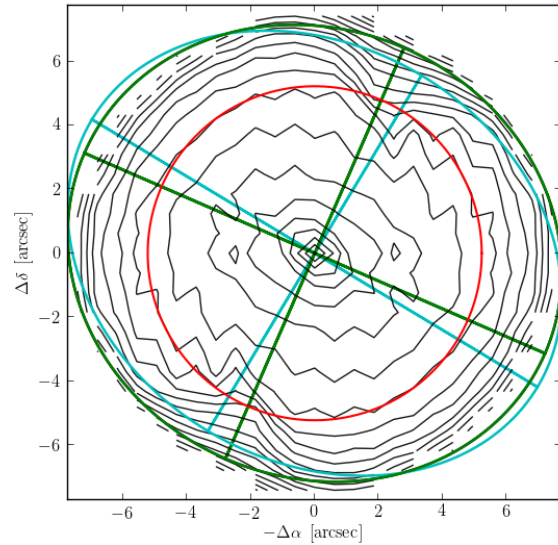


(d)

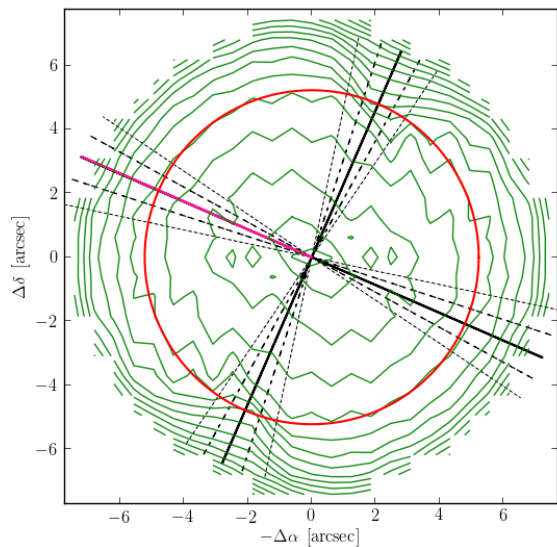
Figure 9: Reconstruction of lens *BRI0952*. Analogous to Figure 1.



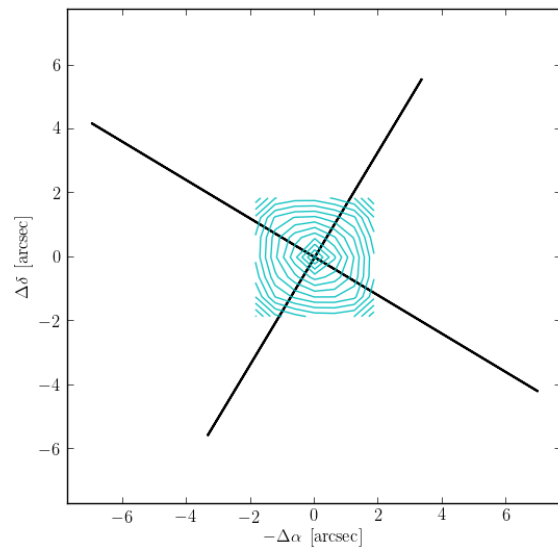
(a)



(b)

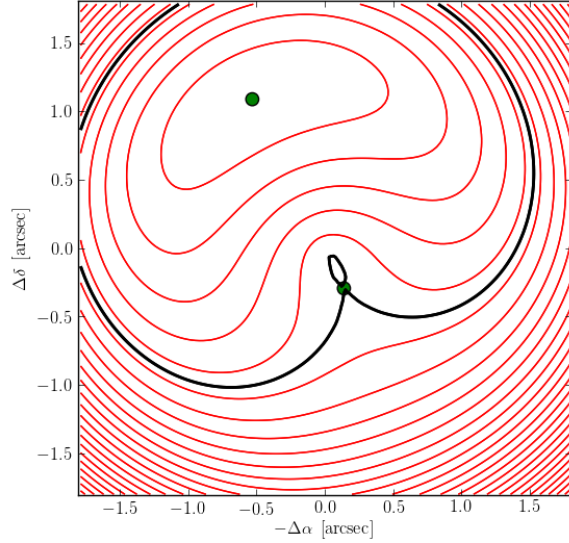


(c)

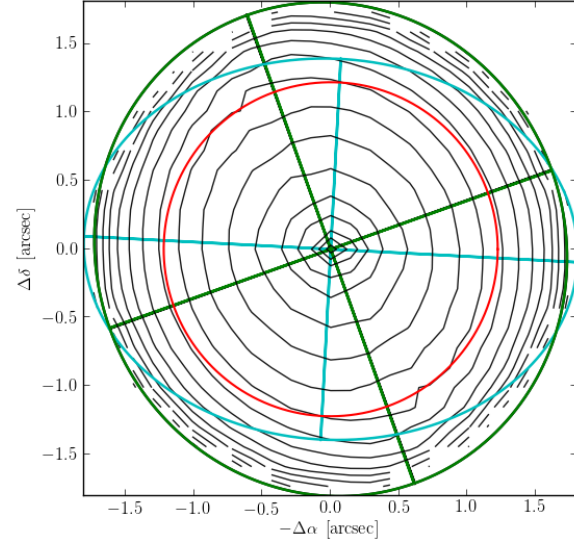


(d)

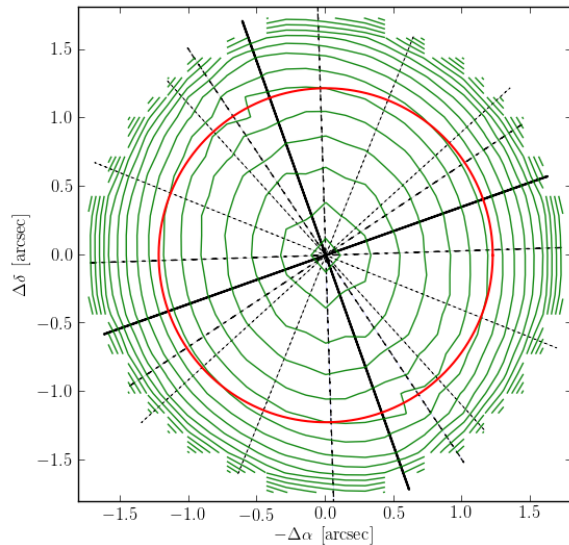
Figure 10: Reconstruction of lens $Q0957$. Analogous to Figure 1.



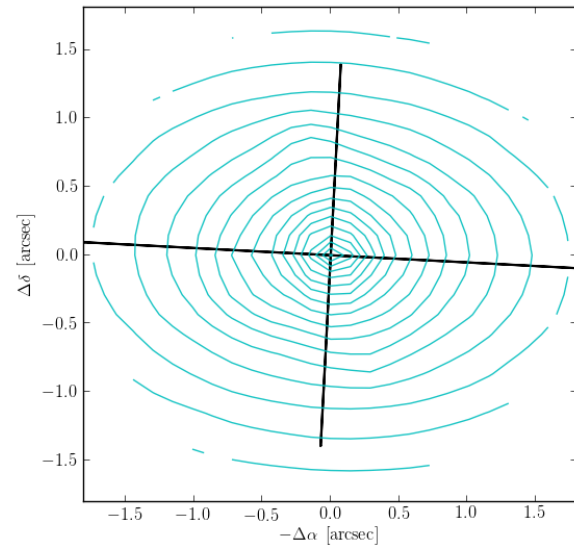
(a)



(b)

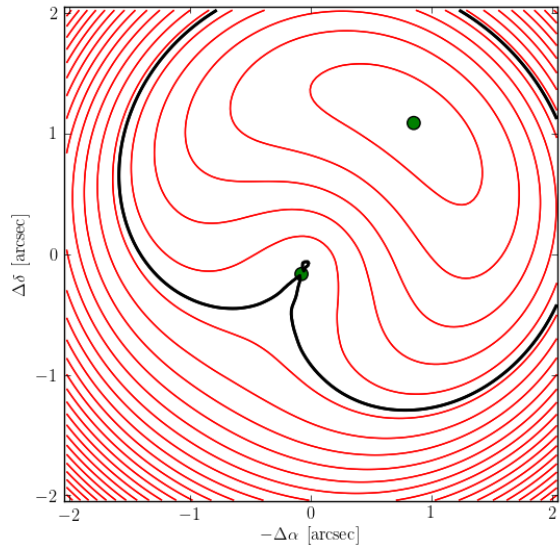


(c)

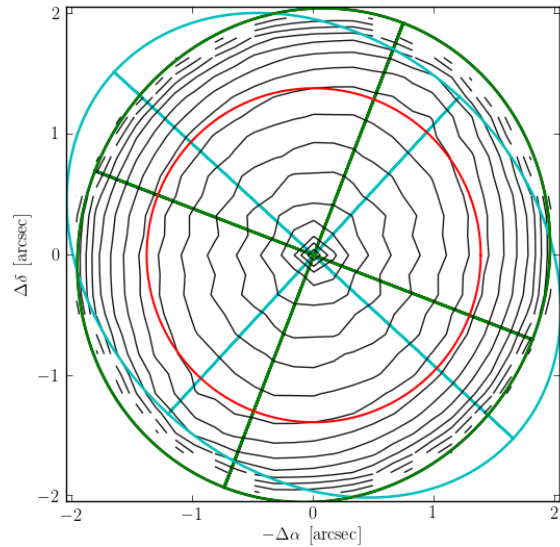


(d)

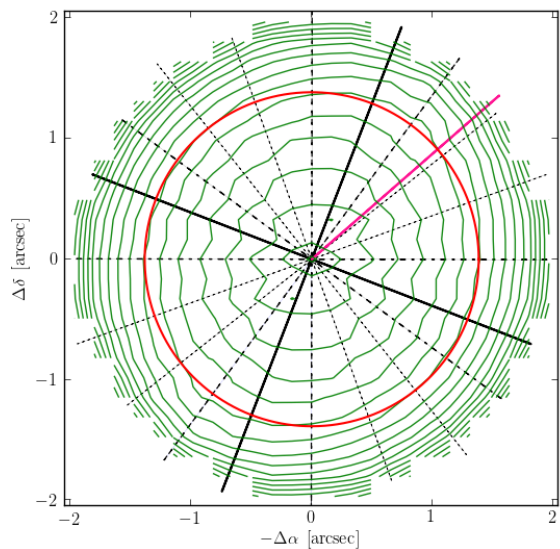
Figure 11: Reconstruction of lens *LBQS1009*. Analogous to Figure 1.



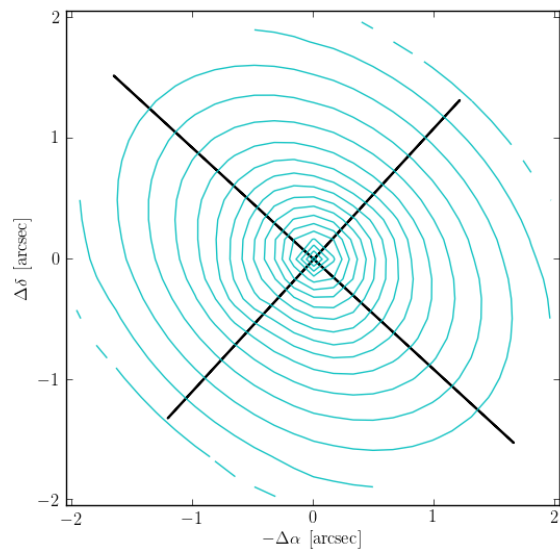
(a)



(b)

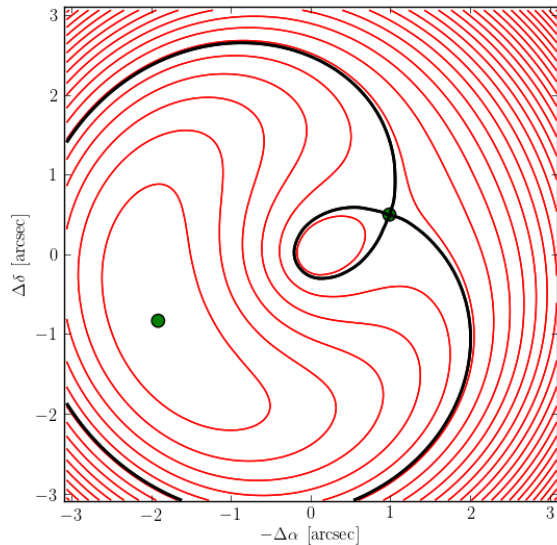


(c)

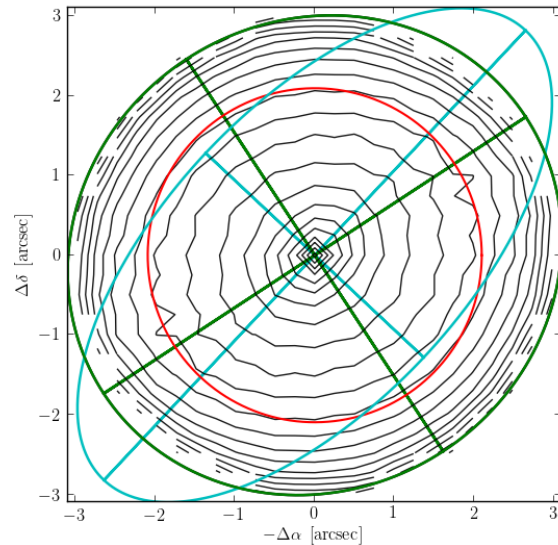


(d)

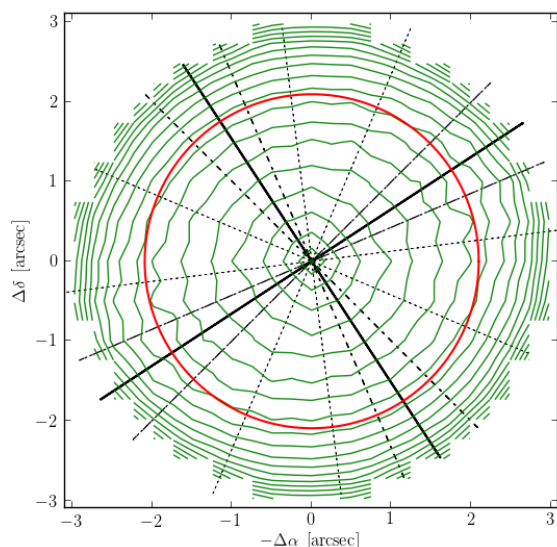
Figure 12: Reconstruction of lens *B1030*. Analogous to Figure 1.



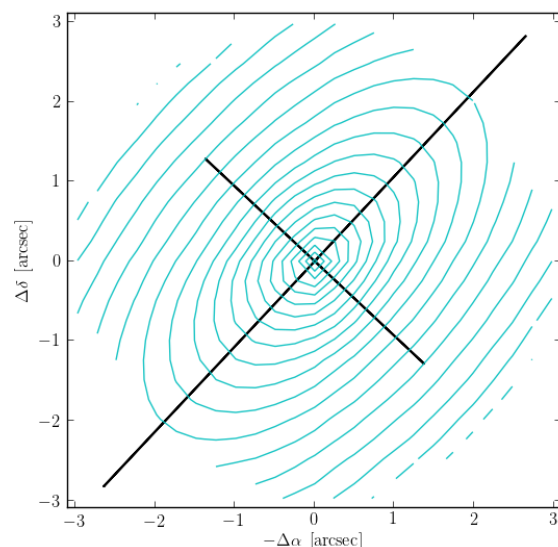
(a)



(b)

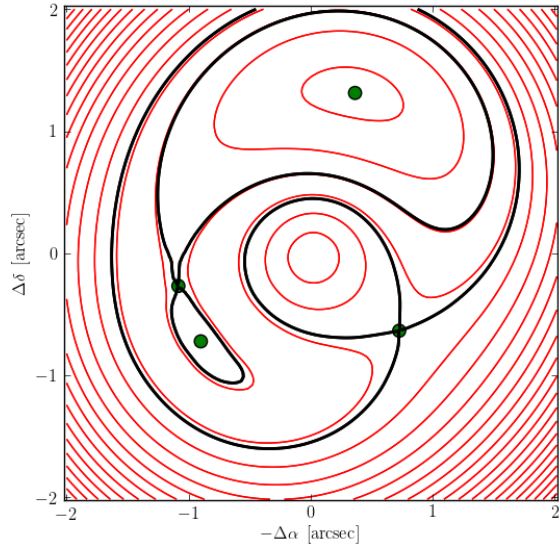


(c)

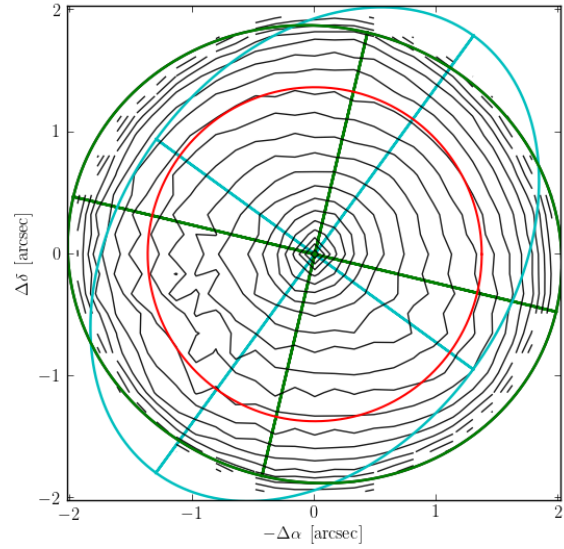


(d)

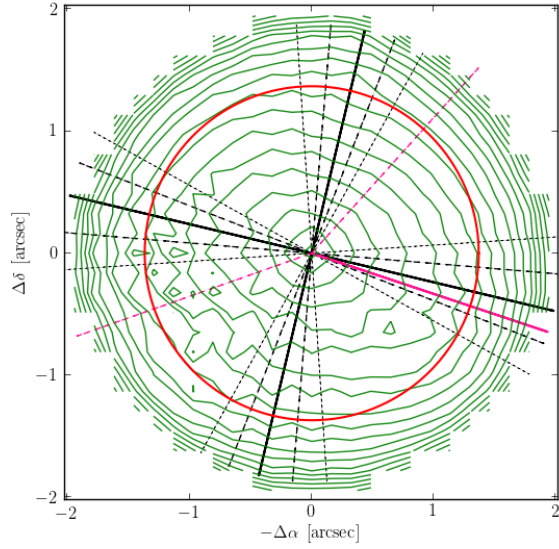
Figure 13: Reconstruction of lens HE1104. Analogous to Figure 1.



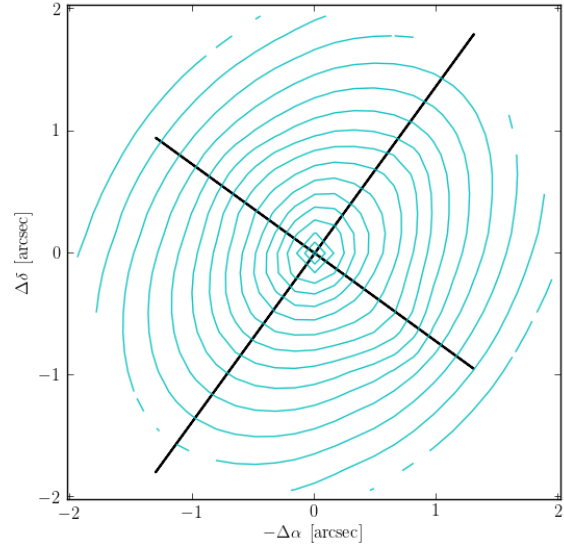
(a)



(b)

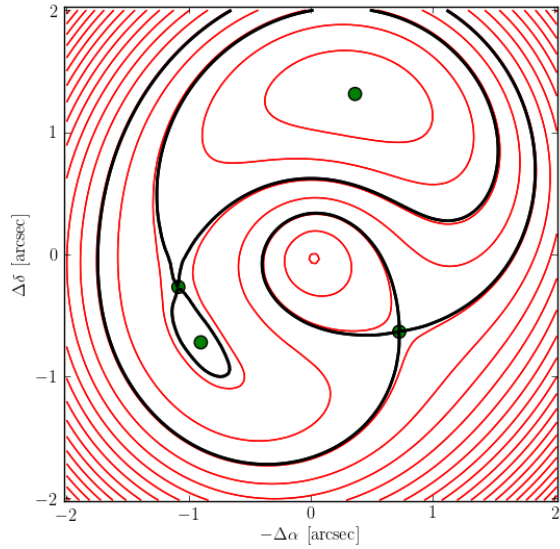


(c)

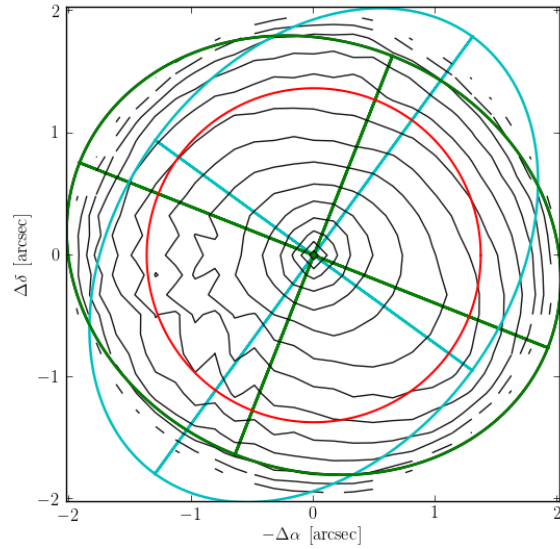


(d)

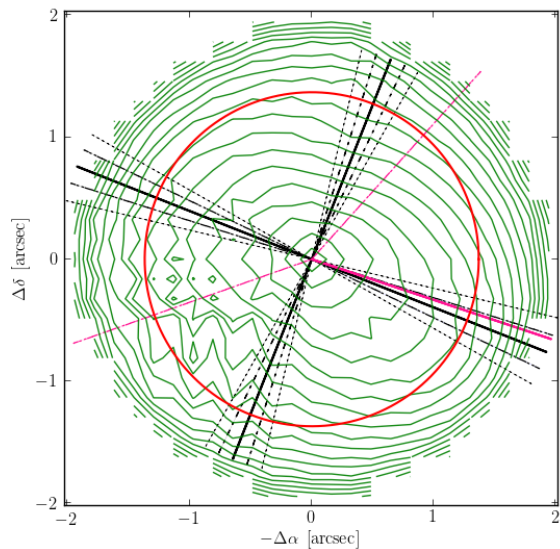
Figure 14: Reconstruction of lens *PG1115* with time delays from Tsvetkova et al. (2010). Analogous to Figure 1.



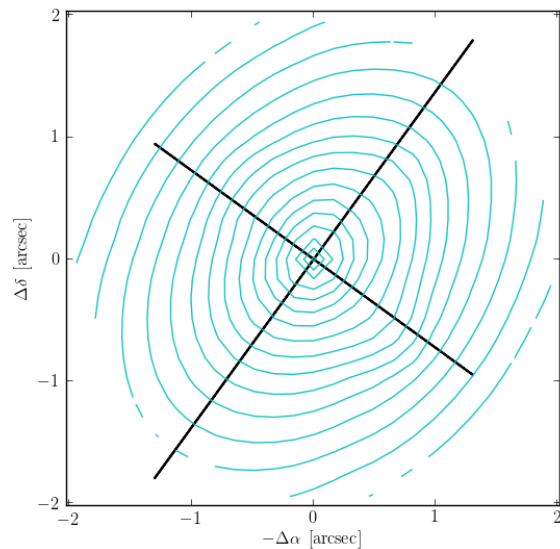
(a)



(b)

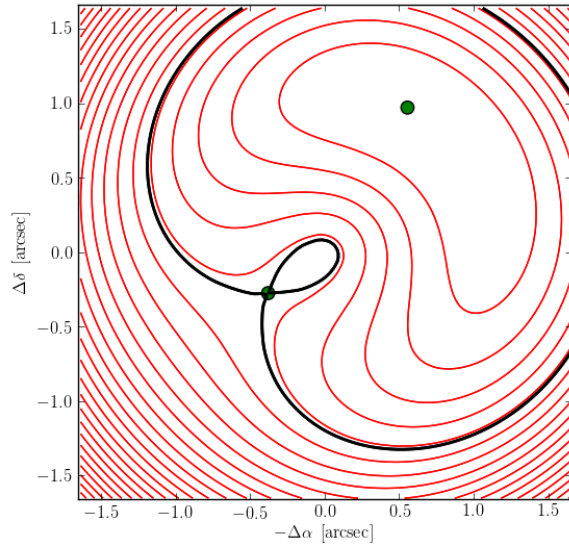


(c)

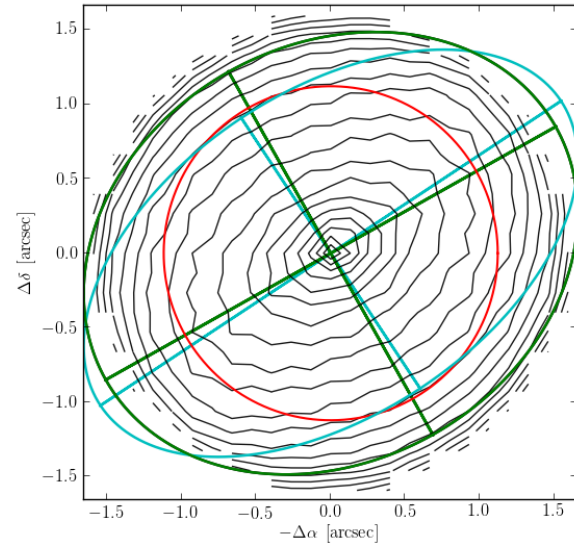


(d)

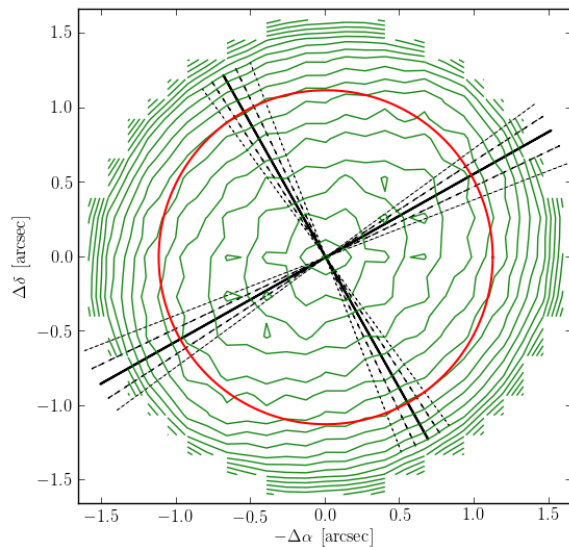
Figure 15: Reconstruction of lens *PG1115* with time delays from Barkana (1997). Analogous to Figure 1.



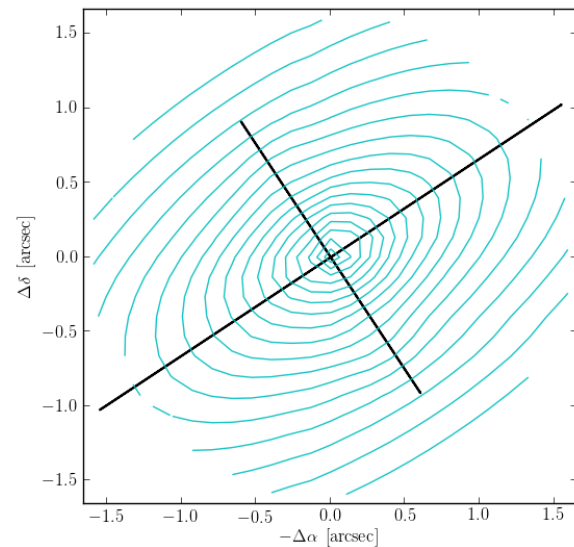
(a)



(b)

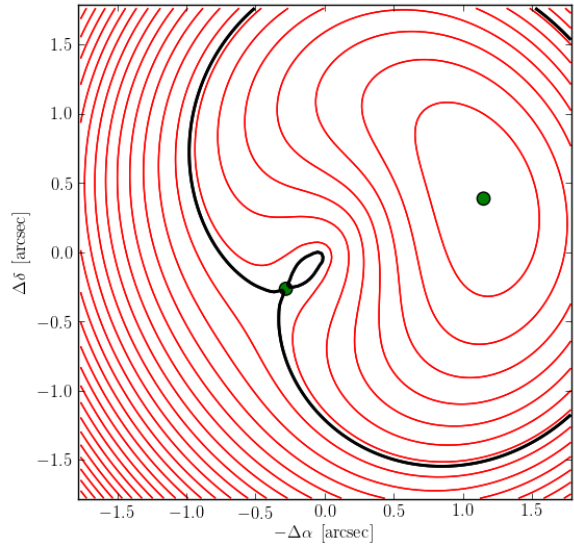


(c)

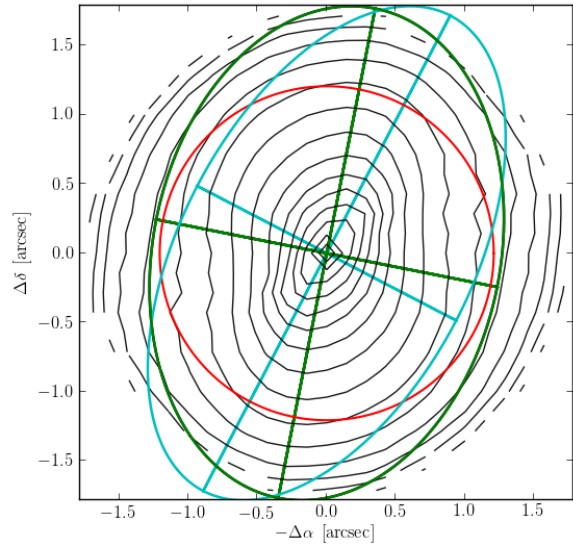


(d)

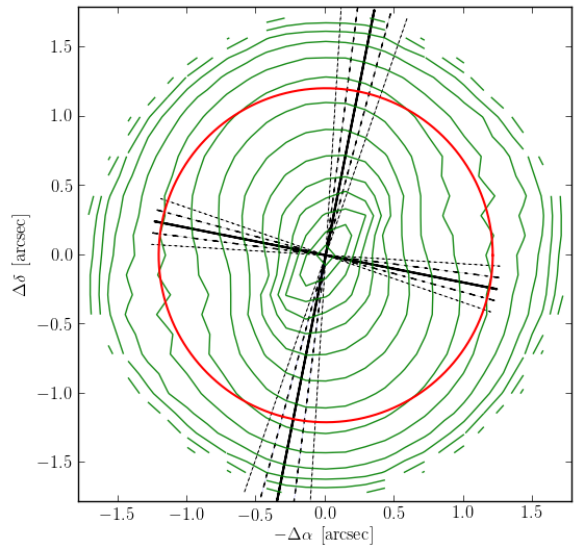
Figure 16: Reconstruction of lens *B1152*. Analogous to Figure 1.



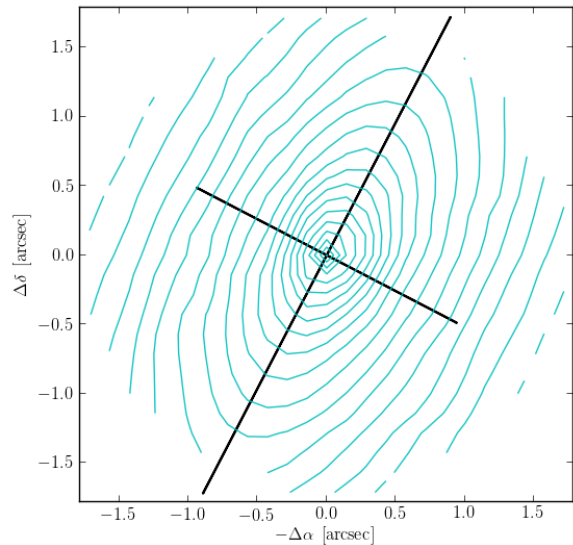
(a)



(b)

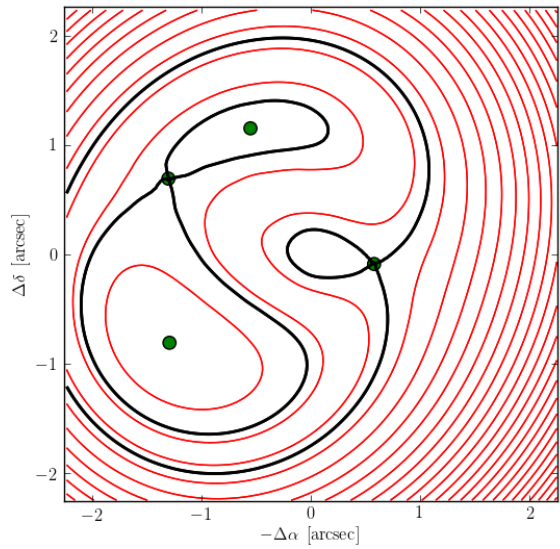


(c)

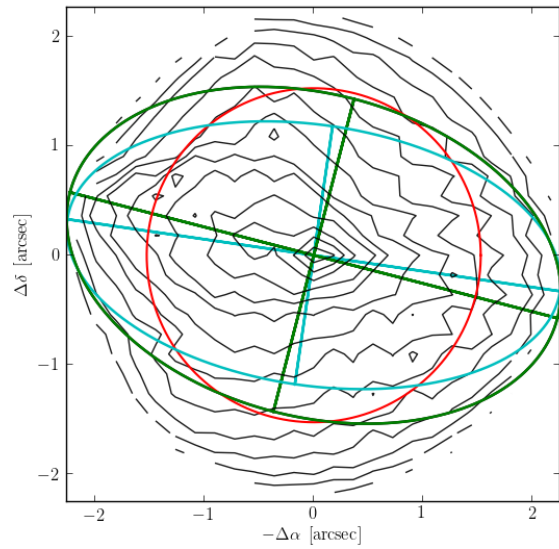


(d)

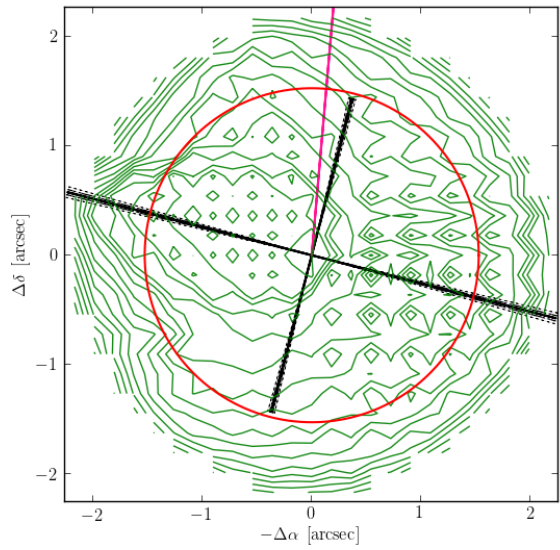
Figure 17: Reconstruction of lens *SBS1520*. Analogous to Figure 1.



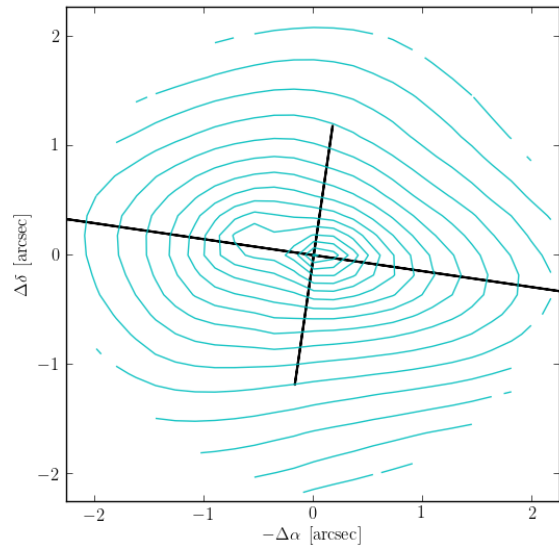
(a)



(b)

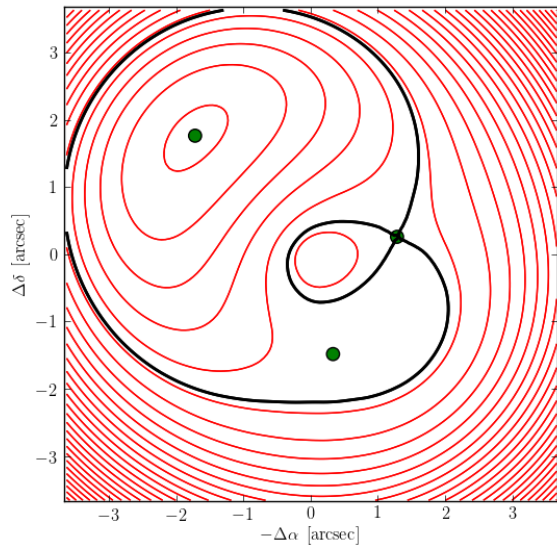


(c)

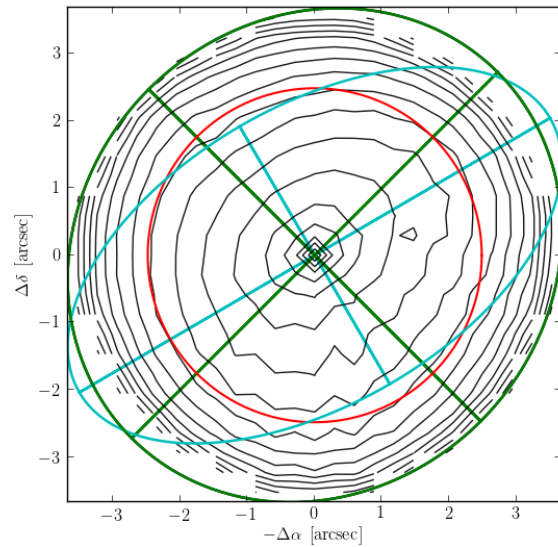


(d)

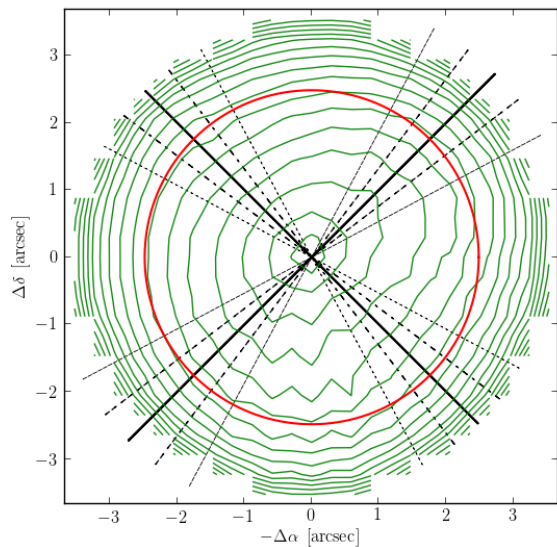
Figure 18: Reconstruction of lens *B1608*. Analogous to Figure 1.



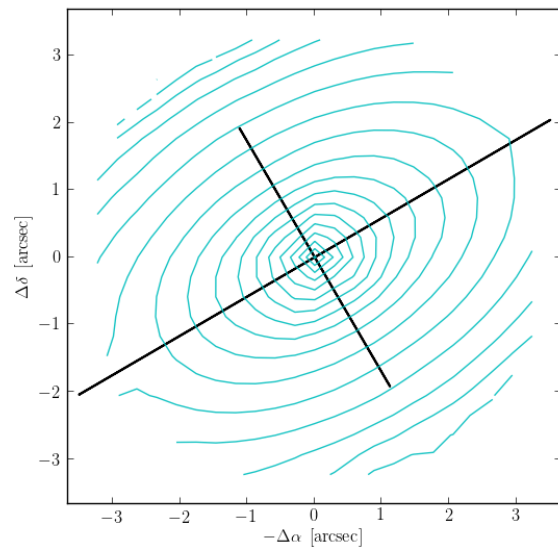
(a)



(b)

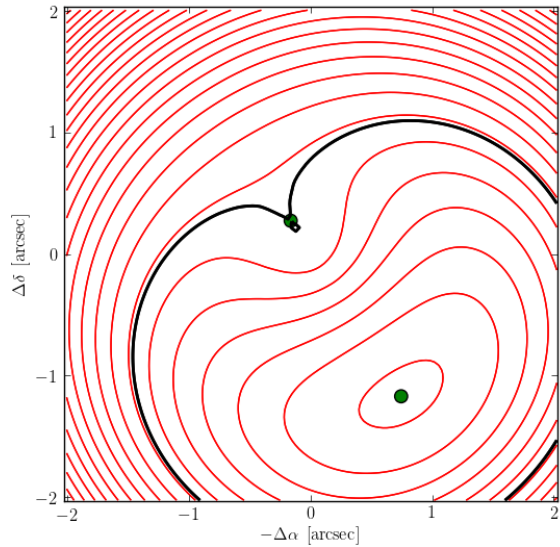


(c)

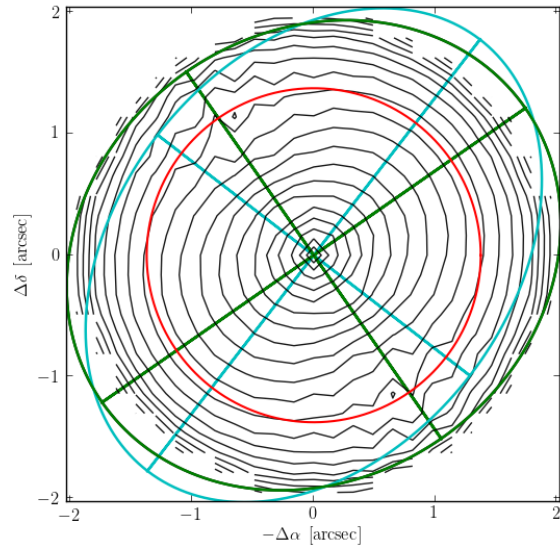


(d)

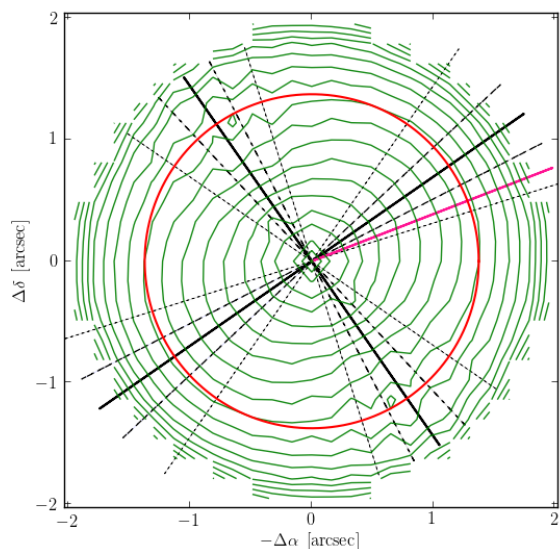
Figure 19: Reconstruction of lens MG2016. Analogous to Figure 1.



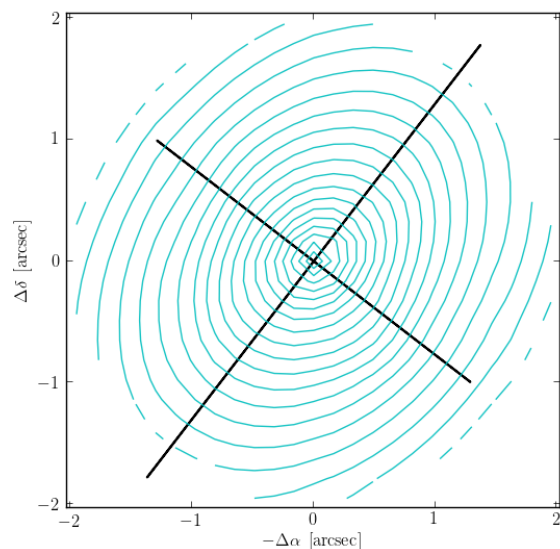
(a)



(b)

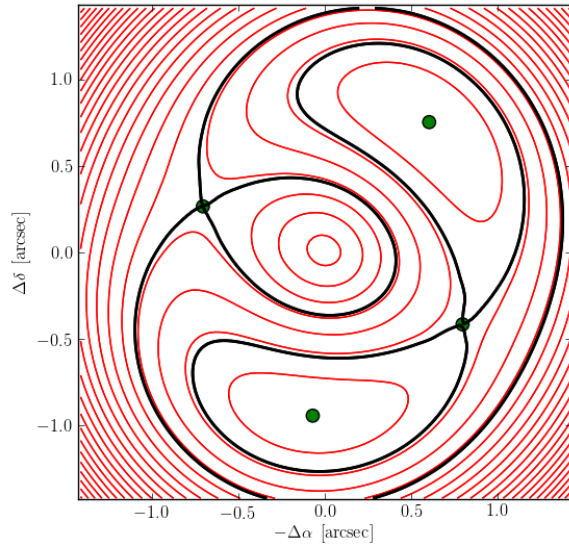


(c)

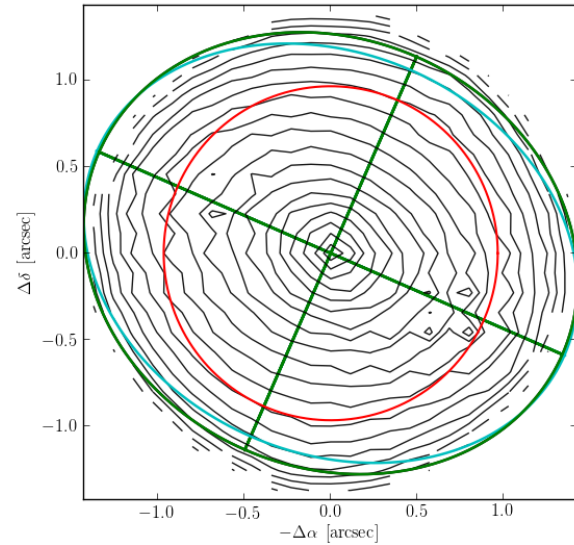


(d)

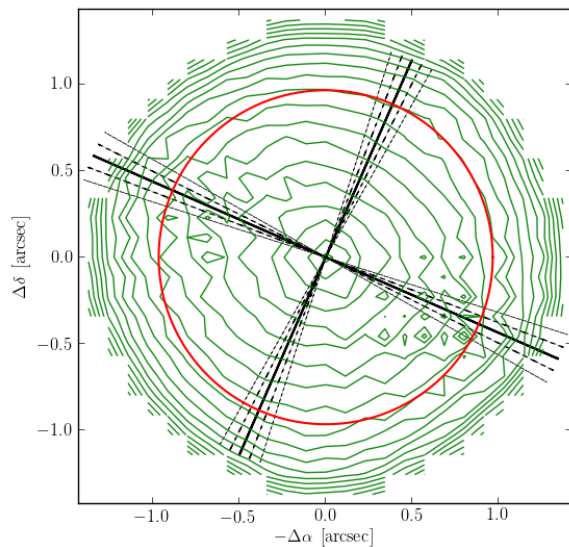
Figure 20: Reconstruction of lens HE2149. Analogous to Figure 1.



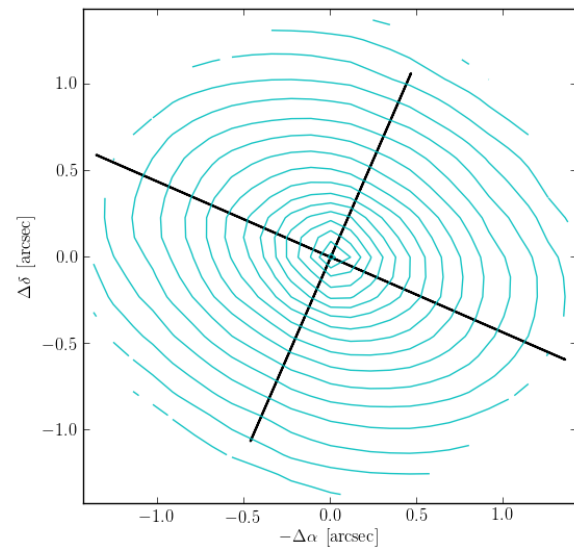
(a)



(b)



(c)



(d)

Figure 21: Reconstruction of lens $Q2237$. Analogous to Figure 1.